# Meta-analysis of Cryogenian through modern quartz microtextures reveals sediment transport histories

**Jocelyn N. Reahl[1]*, Marjorie D. Cantine[1], Julia Wilcots[1], Tyler J. Mackey[1]**, Kristin D. Bergmann[1]**

*[1]Massachusetts Institute of Technology, Department of Earth, Atmospheric, and Planetary Sciences, Cambridge, Massachusetts, 02139 U.S.A.*
**Now at the California Institute of Technology, Division of Geological and Planetary Sciences, Pasadena, California 91125, U.S.A.*
***Now at the University of New Mexico, Department of Earth and Planetary Sciences, Albuquerque, New Mexico 87131, U.S.A.*

Corresponding author: Jocelyn N. Reahl (jreahl@caltech.edu)

## ABSTRACT

Quantitative scanning electron microscopy (SEM) quartz microtextural analysis can reveal the transport histories of modern and ancient sediments. However, because workers identify and count microtextures differently, it is difficult to directly compare quantitative microtextural data analyzed by multiple workers. As a result, the defining microtextures of certain transport modes and their probabilities of occurrence are not well constrained. We used principal component analysis (PCA) to directly compare modern and ancient aeolian, fluvial, and glacial samples from the literature with 9 new samples from active aeolian and glacial environments. Our results demonstrate that PCA can group microtextural samples by transport mode and identify the microtextures that differentiate between aeolian and fluvial/glacial transport modes, regardless of study. The PCA ordinations indicate that aeolian samples are distinct from fluvial and glacial samples, which are in turn difficult to disambiguate from each other. The ancient and modern sediments are also shown to have quantitatively similar microtextural relationships. Therefore, PCA may be a useful tool to constrain the ambiguous transport histories of some ancient sediment grains. As a case study, we analyzed two samples with ambiguous transport histories from the Cryogenian Bråvika Member (Svalbard). Integrating PCA with field observations, we find evidence that the Bråvika Member facies investigated here includes aeolian deposition and may be analogous to syn-glacial Marinoan aeolian units including the Bakoye Formation in Mali and the Whyalla Sandstone in South Australia.


## INTRODUCTION

Scanning electron microscopy (SEM) quartz microtextural analysis reveals microscale features (microtextures) that are formed as quartz grains are transported through sedimentary systems (Krinsley and Takahashi 1962; Krinsley and Doornkamp 1973; Bull 1981). Because different transport modes imprint specific suites of microtextures onto quartz grains, quartz microtextural analysis is a useful technique to understand the transport histories of modern and ancient sedimentary deposits (Krinsley and Doornkamp 1973; Mahaney 2002; Vos et al. 2014). Quantitative quartz microtextural analysis, which treats microtextural data as a multidimensional statistical problem, is a particularly promising method to quantify the probabilities of occurrence of each microtexture in a specific transport mode (Mahaney et al. 2001). However, because workers identify and count microtextures differently—even for sand grains from the same depositional environment (Culver et al. 1983)—it is difficult to directly compare quantitative microtextural data analyzed by more than one worker in the same reference frame. As a result, the defining microtextures of certain transport modes and their probabilities of occurrence are not well constrained.

Here we use principal component analysis (PCA) to directly compare quantitative microtextural data from modern and ancient aeolian, fluvial, and glacial sediments across workers. Because experimental studies have shown that certain microtextures form in specific transport settings (Krinsley and Takahashi 1962; Lindé and Mycielska-Dowgiałło 1980; Costa et al. 2012; Costa et al. 2013; Costa et al. 2017), we expect the PCA ordinations to identify the microtextures that distinguish aeolian, fluvial, and glacial sediments from each other regardless of worker. We also hypothesize that the modern and ancient samples will be quantitatively similar to each other in PCA space, and that the depositional histories of ambiguous ancient sedimentary environments can be constrained using this method.

One such case of an ambiguous ancient sedimentary environment is the Cryogenian (720–635 Ma) Bråvika Member. The Bråvika Member is a northward-thickening and coarsening-upward wedge of quartz arenite with lenses and beds of dolomite that outcrop in northeastern Svalbard, Norway (Halverson et al. 2004). Since the Bråvika Member was first recognized as a unit by Halverson et al. (2004), there have been three prevailing hypotheses for what depositional environment the Bråvika could represent: 1) a glaciofluvial outwash plain associated with the overlying Wilsonbreen Formation (Halverson et al. 2004), which is correlated with the Marinoan "Snowball Earth" pan-glaciation (Hoffman et al. 2012); 2) an aeolian depositional environment associated with either the glacial conditions of the Wilsonbreen Formation or the tropical equatorial conditions of the underlying upper Elbobreen Formation (Halverson 2011), the latter of which is correlated with the Cryogenian interglacial period (Fairchild et al. 2016); and 3) a tropical fluvial environment associated with the upper Elbobreen Formation (Hoffman et al. 2012). This ambiguous depositional history makes it a target for a microtextural case study.

To test if our PCA analysis method can constrain the transport histories of ambiguous ancient sedimentary environments, we transformed two microtextural samples of the Bråvika Member from Buldrevågen (North-Northeast Spitsbergen) into the PCA ordinations. Integrating the microtextural data with field observations from Buldrevågen, Geerabukta (Ny Friesland), and Gimleodden (Nordaustlandet), we show that microtextural PCA is not only able to identify the distinguishing microtextures of aeolian, fluvial, and glacial transport modes, but it is also able to help elucidate the ambiguous transport histories of ancient sediment grains.

## MATERIALS

### *Modern Samples*

**Lake Fryxell, Lake Joyce, and Lake Vanda, McMurdo Dry Valleys, Antarctica. —–** We analyzed aeolian sand samples sourced from three lakes in the McMurdo Dry Valleys in Antarctica: Lake Fryxell (documented in Jungblut et al. 2016), Lake Joyce (documented in Mackey et al. 2015), and Lake Vanda (documented in Mackey et al. 2017; Fig. 1; Table 1). All three of these lakes are perennially ice-covered, closed-basin lakes with persistent, salinity-dependent density gradients due to a lack of wind-driven turbulence (Spigel and Priscu 1998). The stability of these environments and persistent ice cover suggest that very limited sediment transport and erosion occurs within these lakes. Therefore, sand grains deposited in these lakes are expected to retain microtextural characteristics from their transport history into the lake, without subsequent overprinting. The bulk of coarse-grained sedimentation under the ice cover of these lakes is wind-blown sand that melts through the ice and is deposited within layers of microbial mats on the lake floor (Nedell et al. 1987; Rivera-Hernandez et al. 2019). The sand is

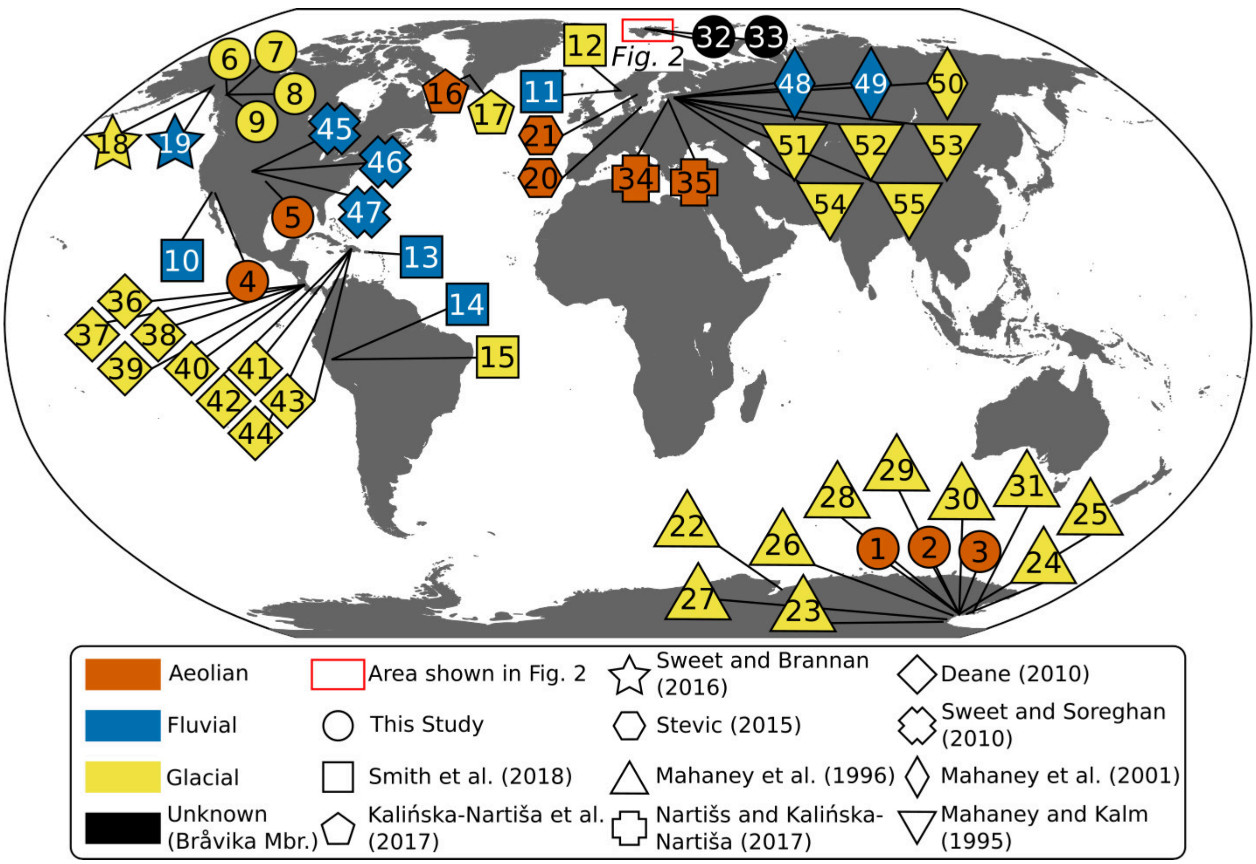


**Figure 1.** Global map of all samples analyzed in this study. The number in each marker corresponds to the sample group number in Tables 1 and 2.

mineralogically similar to the surrounding exposed bedrock in the Dry Valleys and is most likely sourced from reworked glacial tills and bedrock outcrops of the Beacon Sandstone and the Ferrar Dolerite (Gumbley 1975).

**Algodones Dunes, Imperial Sand Dunes Recreational Area, California, U.S.** —– We analyzed one sample of aeolian sand (described in Adams 2018; Adams and Soreghan 2020) from the northwest region of the Algodones Dunes in the Imperial Sand Dunes Recreational Area of southeastern California, on the territories of the Cocopah (*Kwapa*), Kumeyaay, Salt River Pima-Maricopa (*O'odham-Piipaash*), and Quechan (*Kwatsáan*) (Fig. 1; Table 1). The Algodones Dunefield stretches 80 km along a northwestern to southeastern path (reflecting the northwesterly prevailing winds) and ranges in width from 3 km in the northwest to 10 km in the southeast (Muhs et al. 1995; Derickson et al. 2008; Adams 2018). The dunefield is positioned along the eastern margin of the tectonically active Salton Trough, which is a major basin filled with 3-6 km of Miocene and younger sediment mostly deposited by the Colorado River (Axen and Fletcher 1998; Derickson et al. 2008). Many workers (Norris and Norris 1961; McCoy et al. 1967; Van de Kamp 1973; Winspear and Pye 1995) have suggested that the Algodones Dunes are sourced from the shores of the ancient Lake Cahuilla, which was a series of lakes that were created when the Colorado River periodically diverted into the Salton Trough (Waters 1983).

**Table 1.** List of the samples from modern depositional environments considered in this study. Each group of samples is assigned a number for later reference in Figures 1 and 5 (Column #). Column S indicates the number of samples in each sample group, and column N indicates the number of quartz grains in each sample group.

| Study | # | Sample Location | Transport | S | N | GPS Point |
|---|---|---|---|---|---|---|
| This Study | 1 | Lake Fryxell, McMurdo Dry Valleys, Antarctica | Aeolian | 1 | 31 | 77°36'48"S, 163°06'40"E |
| | 2 | Lake Joyce, McMurdo Dry Valleys, Antarctica | Aeolian | 1 | 34 | 77°43'11"S, 161°36'25"E |
| | 3 | Lake Vanda, McMurdo Dry Valleys, Antarctica | Aeolian | 1 | 30 | 77°31'38"S, 161°36'24"E |
| | 4 | Algodones Dunes, California, U.S. | Aeolian | 1 | 44 | 33°08'57"N, 115°18'48"W |
| | 5 | Waynoka Dunes, Oklahoma, U.S. | Aeolian | 1 | 48 | 36°33'35"N, 98°53'56"W |
| | 6 | Llewellyn Glacier, B.C. (JIF19-C26-01) | Glacial | 1 | 31 | 59°00'49"N, 134°07'15"W |
| | 7 | Llewellyn Glacier, B.C. (JIF19-C26-02) | Glacial | 1 | 39 | 59°00'48"N, 134°07'13"W |
| | 8 | Llewellyn Glacier, B.C. (JIF19-C26-03) | Glacial | 1 | 36 | 59°00'48"N, 134°07'13"W |
| | 9 | Llewellyn Glacier, B.C. (JIF19-C26-04) | Glacial | 1 | 40 | 59°00'50"N, 134°07'14"W |
| Smith et al. (2018) | 10 | Anza-Borrego Desert, California, U.S. | Fluvial | 5 | 250 | 32°54'00"N, 116°16'00"W |
| | 11 | Auster and Storelvi Rivers, Norway | Fluvial | 7 | 346 | 61°32'00"N, 06°57'00"E |
| | 12 | Austerdal Glacier Moraine, Norway | Glacial | 1 | 50 | 61°32'00"N, 06°57'00"E |
| | 13 | Rio Guayanés, Puerto Rico | Fluvial | 6 | 297 | 18°03'00"N, 65°54'00"W |
| | 14 | Rio Parón, Peru | Fluvial | 5 | 250 | 09°00'00"S, 77°42'00"W |
| | 15 | Moraine Proximal to Lake Parón, Peru | Glacial | 1 | 48 | 09°00'00"S, 77°42'00"W |
| Kalińska-Nartiša et al. (2017) | 16 | Russell Glacier, Greenland (CE1, CE2, CE8) | Aeolian | 3 | 60 | 67°05'00"N, 50°20'00"W |
| | 17 | Russell Glacier, Greenland (CE12, CE13) | Glacial | 2 | 40 | 67°07'00"N, 50°05'00"W |
| Sweet and Brannan (2016) | 18 | Chitina Glacier Moraine to 12 km Past Tana River Confluence, Alaska, U.S. (CR-1 to CR-23) | Glacial | 22 | 626 | 61°05'44"N, 142°11'03"W |
| | 19 | 12 km Past Tana River Confluence to the Copper River, Alaska, U.S. (CR-24 to CR-41) | Fluvial | 18 | 450 | 61°21'42"N, 143°46'34"W |
| Stevic (2015) | 20 | Coastal Sand Dune, Vittskövle, Sweden | Aeolian | 1 | 15 | 55°51'56"N, 14°10'02"E |
| | 21 | Inland Sand Dune, Brattforsheden, Sweden | Aeolian | 1 | 15 | 59°36'26"N, 13°53'03"E |
| Mahaney et al. (1996) | 22 | Lichen Valley, Vestfold Hills, Antarctica (Site A) | Glacial | 1 | 25 | 68°28'53"S, 78°10'24"E |
| | 23 | Ackerman Ridge, Scott Glacier area, Antarctica (Sites B – C) | Glacial | 1 | 25 | 85°45'00"S, 153°00'00"W |
| | 24 | Southern Inexpressible Island, Antarctica (Site D) | Glacial | 1 | 25 | 74°54'00"S, 163°39'00"E |
| | 25 | Taylor Glacier, McMurdo Dry Valleys, Antarctica (Site E) | Glacial | 1 | 25 | 77°44'00"S, 162°10'00"E |
| | 26 | Hatherton Glacier, Antarctica (Site F) | Glacial | 1 | 25 | 79°55'00"S, 157°35'00"E |
| | 27 | Roberts Massif, Antarctica (Sites G – H) | Glacial | 2 | 50 | 85°32'00"S, 177°05'00"W |
| | 28 | Barwick Valley, Antarctica (Site I) | Glacial | 1 | 25 | 77°23'24"S, 161°02'18"E |
| | 29 | Cambridge Glacier, Antarctica (Site J) | Glacial | 1 | 25 | 76°57'00"S, 160°31'00"E |
| | 30 | Southern Inexpressible Island, Antarctica (Site D) | Glacial | 1 | 25 | 75°38'00"S, 161°05'00"E |
| | 31 | Luther Peak Basin, Edisto Inlet, Antarctica (Site L) | Glacial | 1 | 25 | 72°22'00"S, 169°50'00"E |

**Waynoka Dunes, Little Sahara State Park, Oklahoma, U.S.** —– We analyzed one sample of aeolian sand (described in Adams 2018; Adams and Soreghan 2020) from the northwest region of the Waynoka Dunes in the Little Sahara State Park of west-central Oklahoma on the territories of the Comanche (*Nʉmʉnʉʉ*), Kiowa (*[Gáui[dòñ:gyà*), Osage (*Wahzhazhe*), Wichita (*Kirikirʔi:s*), Waco (*Wí:koʔ*), Keechi (*Ki:che:ss*), and Tawakoni (*Tawá:kharih*) (Fig. 1; Table 1). The Waynoka Dunes form part of the Cimarron River Valley dune system, which was formed by the aeolian erosion of Quaternary sandy river terraces left behind by the Cimarron River (Cimarron *Nahe:hah* in Wichita) as it migrated towards the southwest (Madole et al. 1991; Lepper and Scott 2005). The Waynoka Dunes were active as recently as the 1930s Dust Bowl (Rogers 2007), but vegetation has since stabilized most of the dunes (Adams 2018). However, the dunes in the Little Sahara State Park remain unvegetated due to continuous motorized vehicle usage (Adams 2018).

**Llewellyn Glacier, Juneau Icefield, Northwestern British Columbia, Canada. ––** We analyzed four glacial samples from a nunatak on the Llewellyn Glacier (Llewellyn *Sít'* in the Tlingit language) in the Coast Range of northwestern British Columbia, Canada, in the heart of Taku River Tlingit (*Lingít*) First Nation territory (Fig. 1; Table 1). Tlingit people occupied this territory before and after European colonization and live on this land to the present day. The Llewellyn Glacier is a northward-flowing outlet glacier of the Juneau Icefield, flowing about 30 km east-northeast from peaks up to 2300 m to a terminus (*a shuyee*) at 730 m near the southern end of Atlin Lake (*Áa Tlein*; Clague et al. 2010). The nunataks (exposed bedrock surrounded by ice) in this region are predominantly composed of schist, gneiss, quartzite, and marble of the Nisling assemblage (Brew et al. 1991). Prior to the 1990s, a branch of the Llewellyn Glacier eroded a section of nunatak near Camp 26, a camp established and maintained by the Juneau Icefield Research Program. However, as regional annual temperatures rose, the branch became separated from the thinning Llewellyn Glacier and began to melt as "dead ice" (inactive glacier ice). Over the course of 30 years, the melting dead ice has revealed readily accessible lateral moraines and created active glaciofluvial melt streams in the summer (S. McGee *pers. comm.* 2019). Of the four glacial sediment samples collected at this location, two samples (JIF19-C26-01 and JIF19-C26-04) were collected from a glaciofluvial melt stream 10 m downstream from the dead ice, and the remaining samples (JIF19-C26-02 and JIF19-C26-03) were collected from recently-inactive lateral moraines. Because many kilometers of fluvial transport are needed to create a fluvial microtextural overprint on glacial sediment (Pippin 2016; Sweet and Brannan 2016; Křížek et al. 2017), samples JIF19-C26-01 and JIF19-C26-04 are more representative of a glacial setting than a fluvial setting.

**Modern Literature Samples. ––** Previously published aeolian, fluvial, and glacial samples comprise the remainder of modern samples considered in this study (Fig. 1; Table 1). We selected 5 studies to use in this modern dataset: Mahaney et al. (1996), Stevic (2015), Sweet and Brannan (2016), Kalińska-Nartiša et al. (2017), and Smith et al. (2018).

Mahaney et al. (1996) analyzed 11 glacial samples distributed around the Antarctic continent.

Stevic (2015) analyzed two aeolian samples, one from a coastal dune in Vittskövle, Sweden and another from an inland sand dune near Brattforsheden, Sweden.

Sweet and Brannan (2016) analyzed 46 samples of sand from the Chitina Glacier (*Tsedi Łuu* in Ahtna Athabascan) to the Copper River (*'Atna'tuu*) on Ahtna Athabascan territory. Sweet and Brannan (2016) investigated the microtextural transition from glacially-dominated samples to fluvially-dominated ones. For the purposes of sorting these samples into *glacial* and *fluvial* bins, we use Sweet and Brannan's (2016) 5-point averaged fluvial-glacial (F/G) microtextural ratio, where fluvial microtextures are features formed via percussion and saltation (edge rounding and v-shaped percussion cracks) and glacial microtextures are features formed in a high-stress environment (crescentic gouges, curved grooves, deep troughs, and straight grooves). Samples with a 5-point averaged F/G > 1 are classified as *fluvial* samples and samples with a 5-point averaged F/G < 1 are classified as *glacial*.

Kalińska-Nartiša et al. (2017) analyzed three aeolian samples and two glacial samples from the Russell Glacier in southwest Greenland on Kalaallit territory.

Finally, Smith et al. (2018) analyzed 25 fluvial and glacial samples from the Anza-Borrego Desert in California (Cocopah, Cahuilla, and Kumeyaay territory), the Auster and Storelvi Rivers in Norway, the Rio Guayanés in Puerto Rico (Játibonicu Taíno territory), and the Rio Parón in Peru (Quechua-Kichwa territory). Because Smith et al. (2018) saw no significant change in percussion features along each of the river transects—even in glaciofluvial settings—the *fluvial* samples in Smith et al. (2018) are defined as those collected along river transects and the *glacial* samples are defined as those collected at moraines.

### *Ancient Samples*

**Cryogenian Bråvika Member, Svalbard, Norway.** —– The Cryogenian Bråvika Member is a northward-thickening and coarsening-upward wedge of quartz arenite with lenses and beds of dolomite that outcrop in northeastern Svalbard, Norway (Halverson et al. 2004; Figs. 1, 2A). The Bråvika Member is situated between two units that are interpreted to represent different Cryogenian climate states (Fig. 2B). The underlying siltstone and dolomite of the upper Elbobreen Formation (MacDonaldryggen and Slangen Members) are correlated with the warm Cryogenian interglacial period (Fairchild et al. 2016), which spanned from the Sturtian deglaciation to the Marinoan glacial initiation. Absolute age constraints on this period are limited, but the Sturtian deglaciation is constrained between >662.7 ± 6.2 Ma (U-Pb SIMS in South China; Yu et al. 2017) to >657.2 ± 2.4 Ma (Re-Os in Southern Australia; Kendall et al. 2006), and the Marinoan glacial onset is constrained between <654.6 ± 3.8 Ma (U-Pb SIMS in South China; Zhang et al. 2008) to >639.29 ± 0.26/0.31/0.75 Ma (U-Pb CA-ID-TIMS in Congo; Prave et al. 2016). The overlying glacial diamictites of the Wilsonbreen Formation share a reciprocal thickness relationship with the Bråvika Member and are correlated with the Marinoan glaciation (Hoffman et al. 2012), which ended between 636.41 ± 0.45 Ma (U-Pb CA-ID-TIMS in Southern Australia; Calver et al. 2013) to >632.3 ± 5.9 Ma (Re-Os in Laurentia; Rooney et al. 2015).

As discussed previously, the Bråvika Member has been interpreted three different ways: 1) a glaciofluvial outwash plain associated with the Wilsonbreen Formation (Halverson et al. 2004); 2) an aeolian depositional environment associated with either the Wilsonbreen Formation or the upper Elbobreen Formation (Halverson 2011); and 3) a tropical fluvial environment associated with the Elbobreen Formation (Hoffman et al. 2012). We analyzed two samples of the Bråvika Member from a site at Buldrevågen in North-Northeast Spitsbergen (Fig. 2A), one at 12 m and another at 22 m above the base of the Bråvika Member (Fig. 2C). We will present field

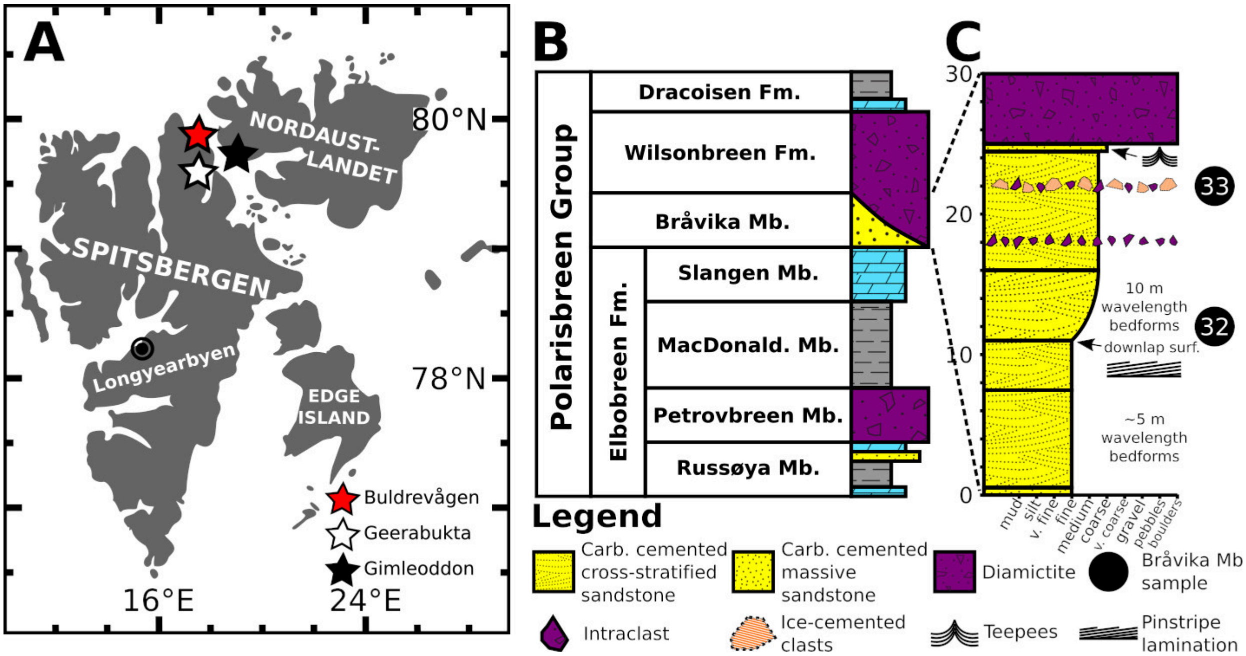


**Figure 2.** Geologic context and stratigraphy of the Cryogenian Bråvika Member in Svalbard. A) Map of the Svalbard archipelago. Each star indicates a site observed in this study: Buldrevågen (red), Geerabukta (white), and Gimleoddon (black). B) Generalized stratigraphic nomenclature for the Cryogenian Polarisbreen Group in Svalbard after Halverson et al. (2018). As shown here, the Bråvika Member is assigned to neither the Wilsonbreen nor the Elbobreen formations, as its assignment is a key question explored in this study. The Petrovbreen Member is correlated with the Sturtian pan-glaciation and the Wilsonbreen Formation is correlated with the Marinoan pan-glaciation (Hoffman et al. 2012). The MacDonaldryggen and Slangen members are correlated with the Cryogenian interglacial (Fairchild et al. 2016). C) Stratigraphic column of the Bråvika Member at Buldrevågen. The black circles indicate where samples 32 (J1701-156) and 33 (J1701-166) were collected for microtextural analysis.

observations of the Bråvika Member from outcrops in Buldrevågen, Geerabukta (Ny Friesland), and Gimleodden (Nordaustlandet) as context for the microtextural samples.

**Ancient Literature Samples.** –– In addition to the two Bråvika Member samples, we compiled a set of ancient aeolian, fluvial, and glacial microtextural samples from 5 studies: Mahaney and Kalm (1995), Mahaney et al. (2001), Deane (2010), Sweet and Soreghan (2010), and Nartišs and Kalińska-Nartiša (2017) (Fig. 1; Table 2).

Mahaney and Kalm (1995) analyzed 23 glacial samples from the Pleistocene Dainava, Ugandi, Varduva, and Latvia Tills in Estonia.

Mahaney et al. (2001), following Mahaney and Kalm (2000), used quantitative microtextural analysis and Eucledian distances to characterize 29 Pleistocene glacial samples, 3 Pleistocene glaciofluvial samples, and 21 Middle Devonian fluvial samples from Estonia. All of these samples were previously collected and analyzed in Mahaney and Kalm (2000).

Deane (2010) compared 9 Last Glacial Maximum (LGM) glaciogenic samples from Costa Rica (Bribri, Brunka, Huetar, and others' territory) with 9 potentially-glaciogenic samples from the Dominican Republic (Taíno territory) and found that the two sample sets were

**Table 2.** List of the samples from ancient depositional environments considered in this study. Each group of samples is assigned a number for reference in Figures 1, 2, and 6 (Column #). Column S indicates the number of samples in each sample group, and column N indicates the number of quartz grains in each sample group.

| Study | # | Sample | Transport | S | N | GPS Point | Geologic Period |
|---|---|---|---|---|---|---|---|
| This Study | 32 | Bråvika Mbr. – Buldrevågen (J1701-156) | Unknown | 1 | 39 | 79°59'29"N, 17°31'20"E | Cryogenian |
| | 33 | Bråvika Mbr. – Buldrevågen (J1701-166) | Unknown | 1 | 40 | 79°59'29"N, 17°31'20"E | |
| Nartišs and Kalińska-Nartiša (2017) | 34 | Middle Gauja Lowland, Latvia (Mielupīte 1.3) | Aeolian | 1 | 16 | 57°30'00"N, 26°00'00"E | Pleistocene |
| | 35 | Middle Gauja Lowland, Latvia (Mielupīte 1.7) | Aeolian | 1 | 18 | 57°30'00"N, 26°00'00"E | |
| Deane (2010) | 36 | Till, Costa Rica (Sample 2) | Glacial | 1 | 300 | 09°29'35"N, 83°29'07"W | Pleistocene |
| | 37 | Till, Costa Rica (Sample 3) | Glacial | 1 | 100 | 09°29'35"N, 83°29'07"W | |
| | 38 | Till, Costa Rica (Sample 4) | Glacial | 1 | 100 | 09°29'35"N, 83°29'07"W | |
| | 39 | Till, Costa Rica (Sample 5) | Glacial | 1 | 100 | 09°29'35"N, 83°29'07"W | |
| | 40 | Till, Costa Rica (Sample 8) | Glacial | 1 | 100 | 09°29'35"N, 83°29'07"W | |
| | 41 | Till, Dominican Republic (Sample 10) | Glacial | 1 | 100 | 19°02'01"N, 71°04'22"W | |
| | 42 | Till, Dominican Republic (Sample 11) | Glacial | 1 | 100 | 19°01'60"N, 71°04'26"W | |
| | 43 | Till, Dominican Republic (Sample 17) | Glacial | 1 | 100 | 19°02'07"N, 71°04'38"W | |
| | 44 | Till, Dominican Republic (Sample 18) | Glacial | 1 | 100 | 19°01'39"N, 71°02'30"W | |
| Sweet and Soreghan (2010) | 45 | Upper Fountain Fm., Colorado, U.S. | Fluvial | 3 | 47 | 38°51'24"N, 104°54'36"W | Pennsylvanian-Lower Permian |
| | 46 | Middle Fountain Fm., Colorado, U.S. | Fluvial | 8 | 125 | 38°51'24"N, 104°54'36"W | |
| | 47 | Lower Fountain Fm., Colorado, U.S. | Fluvial | 4 | 62 | 38°51'24"N, 104°54'36"W | |
| Mahaney et al. (2001) | 48 | Arküla Stage Sandstone, Estonia | Fluvial | 21 | 420 | 58°15'00"N, 26°30'00"E | Middle Devonian |
| | 49 | Glaciofluvial Sand, Estonia | Fluvial | 3 | 60 | 58°15'00"N, 26°30'00"E | Pleistocene |
| | 50 | Till, Estonia | Glacial | 29 | 580 | 58°15'00"N, 26°30'00"E | |
| Mahaney and Kalm (1995) | 51 | Latvia Till, Estonia | Glacial | 5 | 100 | 58°13'28"N, 26°25'16"E | Pleistocene |
| | 52 | Varduva Till, Estonia | Glacial | 5 | 100 | 58°13'28"N, 26°25'16"E | |
| | 53 | Upper Ugandi Till, Estonia | Glacial | 5 | 100 | 58°13'28"N, 26°25'16"E | |
| | 54 | Lower Ugandi Till, Estonia | Glacial | 5 | 100 | 58°13'28"N, 26°25'16"E | |
| | 55 | Upper Dainava Till, Estonia | Glacial | 3 | 60 | 58°13'28"N, 26°25'16"E | |

statistically indistinguishable, supporting a glaciogenic history for the samples from the Dominican Republic. In our study, we include samples from Deane (2010) that were collected directly from known or hypothesized glacial diamicts and moraines in Costa Rica and the Dominican Republic; we did not include samples from glaciolacustrine environments and debris-flows.

Sweet and Soreghan (2010) characterized the equatorial Pennsylvanian-lower Permian Fountain Formation in Colorado (Cheyenne and Ute territory) and found that the formation likely represents a glaciofluvial fan-delta deposit. We classify these samples as *fluvial* samples.

Nartišs and Kalińska-Nartiša (2017) analyzed two aeolian samples from periglacial aeolian dunes associated with the retreat of the Fennoscandian ice sheet after the LGM in Latvia.

## METHODS

### *Field Work and Sample Collecting*

Samples analyzed for the first time in this study were collected over multiple field seasons using a variety of methods. The samples from the McMurdo Dry Valleys were originally collected as microbial mats using the methods described in Mackey et al. (2015; Lake Joyce), Jungblut et al. (2016; Lake Fryxell), and Mackey et al. (2017; Lake Vanda). Samples from the Algodones Dunes and Waynoka Dunes were collected using the methods described in Adams and Soreghan (2020). On the Juneau Icefield, four sand samples of ~50 g each were collected in August 2019 from glacial moraines and a seasonal glaciofluvial melt stream on the Llewellyn Glacier (Camp 26) nunatak. Field work on the Bråvika Member in Buldrevågen, Geerabukta, and Gimleodden was performed in 2017. The Bråvika Member samples used in this study were collected within stratigraphic sections and documented with field observations and photographs.

### *Microtextural Sample Disaggregation and SEM Preparation*

Most samples collected for this study were unconsolidated sediment, but consolidated samples were disaggregated before analysis. Both dolomite-cemented Bråvika Member samples from Svalbard were disaggregated using 1N hydrochloric acid (HCl) at 50°C for 24 hours. Sand samples from Lake Joyce, Lake Fryxell, and Lake Vanda were disaggregated from the microbial mats using 30% hydrogen peroxide ($H_2O_2$) solution at 50°C for 24 hours to remove organics and 1N HCl at 50°C for 24 hours to remove carbonate. After each disaggregation treatment, the samples were thoroughly rinsed and allowed to dry in an oven.

All of the samples were then prepared for blind microtextural analysis in the style of Smith et al. (2018). Samples were distributed into vials and given unique codes unknown to the primary researcher. Under these conditions, the primary researcher was unaware of each sample's name, age, sampling location, and depositional environment during SEM analysis. These blinded conditions were maintained until after each sample's microtextural data were collected.

After sample randomization, each sample was gently wet sieved into a 125 μm – 1 mm grain size fraction and dried in an oven. After drying, the samples were treated with 30% $H_2O_2$ solution at 50°C for 24 hours to remove organics. Samples were then treated with 1N HCl solution for 24 hours at 50°C to remove any remaining carbonate coatings. Neither $H_2O_2$ nor low-concentration HCl at these temperatures and time frames affects quartz microtextures (Pye 1983; Keiser et al. 2015; Smith et al. 2018).

Samples were then treated using the citrate-bicarbonate-dithionite (CBD) method (Janitsky 1986) to remove iron-oxide and manganese-oxide coatings. Between all chemical treatments, the samples were thoroughly rinsed and dried in an oven. These samples were not sonicated to prevent artificially inducing microtextures (Porter 1962).

Following these treatments, 50 grains that appeared to be quartz (e.g. translucent, no obvious cleavage, etc.) were randomly selected from each sample for microtextural analysis using a reflected-light microscope. The selected grains were mounted on an aluminum SEM stub with double-sided carbon tape in a 10x5 grid and then coated with a 5 nm thick platinum-palladium alloy (Pt/Pd; 80/20) sputter coating to prevent charging under the SEM. Although a gold (Au) or gold-palladium alloy (Au/Pd) coating is frequently used for SEM samples (e.g. Vos et al. 2014), Pt/Pd is a better alternative to Au coatings because Pt/Pd coatings have a smaller grain size allowing for higher-resolution analysis (5-10 nm Au vs. 4-8 nm Au/Pd vs. 2-3 nm Pt/Pd; Goldstein et al. 1992).

### *SEM Imaging and Analysis*

Under the SEM, all 50 grains in each sample were photographed at a 30° tilt on a Zeiss FESEM Supra55VP using a secondary electron (SE2) detector at 20 kV EHT. Viewing the grains at a 30° angle helps to identify smaller microtextures that are difficult to identify at a 0° angle (Margolis and Krinsley 1971). During imaging, energy-dispersive spectroscopy (EDS) was used to confirm the composition of each grain. Non-quartz grains were removed from the analysis. After imaging, each grain was analyzed for the presence or absence of 20 microtextures (Fig. 3) according to the methods of Mahaney et al. (2001) and Mahaney (2002). The microtextures are grouped into five bins as defined by Sweet and Soreghan (2010) that mainly differentiate features by formation process: polygenetic, percussion, high-stress, chemical, and grain relief. The following formation descriptions are from Sweet and Soreghan (2010). Polygenetic features are formed through a variety of processes. Percussion features are formed via grain saltation. High-stress features are formed when grains are subjected to high shear stresses. Chemical features are formed via silica dissolution or precipitation. Grain relief refers to the difference between the high and low points on the grain surface.

Grains with extreme diagenetic overprint (e.g. $\geq$ ~90% estimated coverage of diagenetic overprint; Fig. S1) were removed from the sample dataset. The probability of occurrence for each microtexture $p_m$ was calculated using the following equation:

$$p_m = \frac{\sum_{i=1}^{N} m_i}{N} \quad [1]$$

where $m_i$ is the binary value of microtexture $m$ for grain $i$ (where 0 is “absent” and 1 is “present”) and $N$ is the total number of grains in the sample.

Previous microtextural studies have used a range of sample sizes, from less than 20 grains per sample (Krinsley and Funnell 1965; Coch and Krinsley 1971; Blackwelder and Pilkey 1972) to 100 grains or more per sample (Vincent 1976; Setlow 1978; Deane 2010). This study analyzed ≤ 50 grains per sample as a midpoint between these. 50 grains were initially analyzed using the SEM for each sample, but non-quartz grains and diagenetically overprinted grains were removed from the sample dataset, making 50 grains the upper limit for samples in this study. Although it is appropriate to exclude diagenetically overprinted or non-quartz grains from analysis, in some extremely diagenetically overprinted sediments, a small and perhaps unrepresentative group of grains remained. To address this, samples with ≥ 15 eligible quartz grains were considered statistically significant for analysis; samples with < 15 eligible quartz grains were not analyzed. This limit of 15 grains was selected because it is the midpoint of the lower limit recommended sample sizes of Costa et al. (2012), who advocated for a median

| Microtexture | Abbr. | Description | Formation Process | Example Photo | Microtexture | Abbr. | Description | Formation Process | Example Photo |
|---|---|---|---|---|---|---|---|---|---|
| Abrasion Features | af | Rubbed or worn surface | Polygenetic | 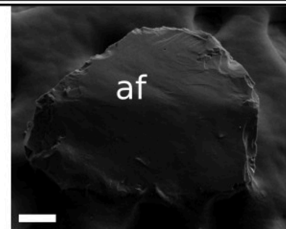 | Linear Steps | ls | Widely spaced linear features, typically > 5 µm apart | Polygenetic | 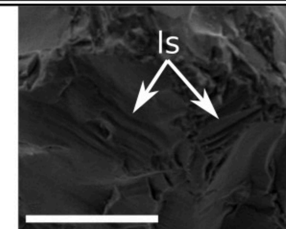 |
| Arc-Shaped Steps | as | Deep tears or breaks caused by impact; Several microns deep and typically spaced > 5 µm apart | Polygenetic | 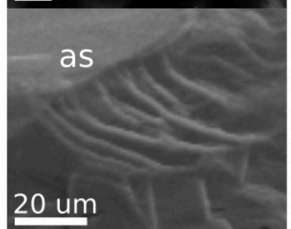 | Sharp Angular Features | saf | Distinct sharp edges on grain surface | Polygenetic | 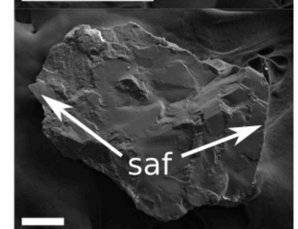 |
| Breakage Blocks | bb | Blocky void marking removal of material, typically along an edge | Polygenetic | 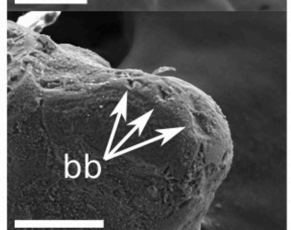 | Subparallel Linear Fractures | slf | Linear fractures, typically < 5 µm spacing | Polygenetic | 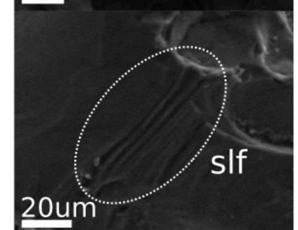 |
| Conchoidal Fractures | cf | Smooth, curved fracture | Polygenetic | 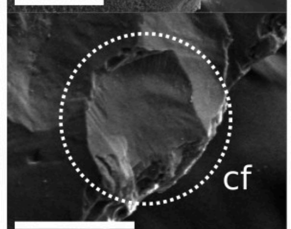 | Edge Rounding | er | Rounded edges on grains | Percussion | 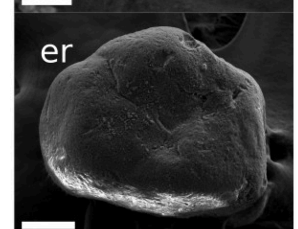 |
| Fracture Faces | ff | Smooth and clean fractures | Polygenetic | 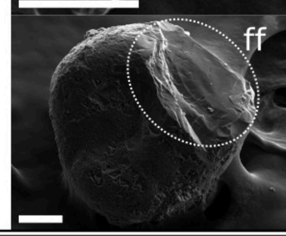 | V-Shaped Percussion Cracks | vc | V-shaped fractures or indentions with typical sizes ranging from 1 µm to 30 µm | Percussion | 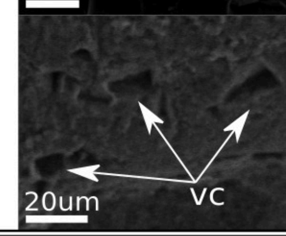 |

**Figure 3A.** Photos and description of microtextures used in this study. Scale bars are 100 µm unless otherwise noted.

| Microtexture | Abbr. | Description | Formation Process | Example Photo | Microtexture | Abbr. | Description | Formation Process | Example Photo |
|---|---|---|---|---|---|---|---|---|---|
| Crescentic Gouges | crg | Crescent-shaped gouges with convex and concave limbs that have depths > 5 μm | High-Stress | 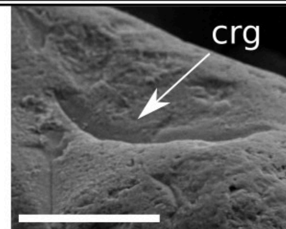  | Dissolution Etching | de | Cavities from chemical dissolution; often crystallo-graphically oriented | Chemical |   |
| Curved Grooves | cg | Curved abrasion feature caused by sustained high-stress contact with another grain, < 5 μm deep | High-Stress | 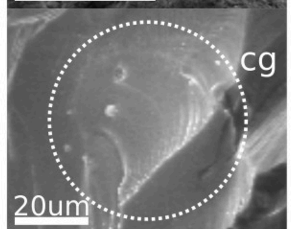  | Precipitation Features | pf | Coatings of amorphous silica precipitation | Chemical | 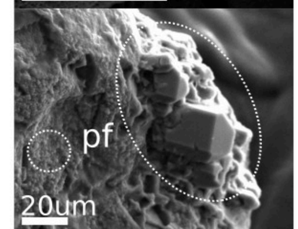  |
| Deep Troughs | dt | Grooves > 10 μm deep | High-Stress | 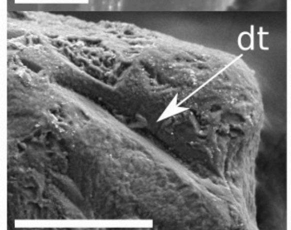  | Low Relief | low | Nearly smooth surface without topographic irregularities | Entire history of grain | 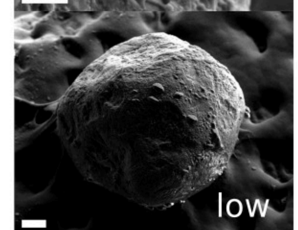  |
| Straight Grooves | sg | Linear grooves < 10 μm deep | High-Stress | 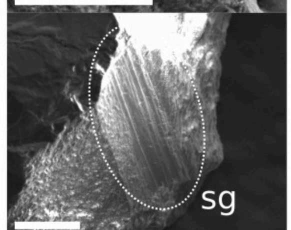  | Medium Relief | med | Semi-smooth surface with topographic irregularities | Entire history of grain | 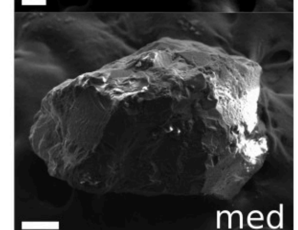  |
| Upturned Plates | up | Surfaces of impact where plates of variable size are partiallly torn from surface, typically > 5 μm | High-Stress | 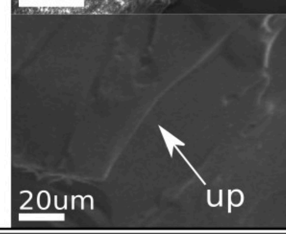  | High Relief | high | Topographically irregular surface with pronounced swells and swales | Entire history of grain | 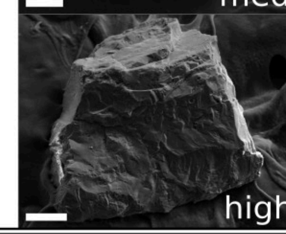  |

**Figure 3B.** Photos and description of microtextures used in this study. Scale bars are 100 μm unless otherwise noted.

number of 20 grains per sample, and of Vos et al. (2014), who advocated for a lower limit of 10 grains per sample.

*Literature Sample Selection*

Because there are differences between authors in experimental design (e.g. number of grains analyzed per sample, number of microtextures counted, type of microtextures counted, etc.; Tables 1–2, S1–S2), modern and ancient samples from the literature (Mahaney and Kalm 1995; Mahaney et al. 1996; Mahaney et al. 2001; Deane 2010; Sweet and Soreghan 2010; Stevic 2015; Sweet and Brannan 2016; Kalińska-Nartiša et al. 2017; Nartišs and Kalińska-Nartiša 2017; Smith et al. 2018) were only incorporated into the study if they met the following criteria: 1) they analyzed sediment transported by aeolian, fluvial, or glacial processes; 2) they analyzed ≥ 15 grains per sample; 3) they used quantitative binary microtextural analysis; and 4) they tabulated at least 75% of the 20 microtextures analyzed in this study (Fig. 3). Microtextures that were similar in appearance and expected provenance but different in name compared to microtextures used in this study (e.g. "linear steps" in this study vs. "straight steps" from Kalińska-Nartiša et al. 2017) were designated as analogs (Table S1–S2). Microtextures that had no analog or were not used in the work's study were not assigned a probability of occurrence, and instead assigned a null value. Nartišs and Kalińska-Nartiša (2017) was the only study to present its data in the form of abundance bins (ex. "abundant" is >75%, "common" is 50-74%, "sparse" is 6-49%, "rare" is <5%, and "not observed" is 0%). These data were plotted using the lowest possible probability for an assigned bin, and sensitivity tests were performed to determine how these samples plot in PCA space using the minimum, median, and maximum probabilities of each abundance bin (Figs. S2–S3).

*Principal Component Analysis (PCA) Comparison*

We preformed PCA analysis on the modern and ancient suites of microtextural data (Scikit-learn 0.21.2; Pedregosa et al. 2011). Two different combinations of microtextures were used to generate PCA axes. The "all-textures" ordination excluded microtextures that were not analyzed by all authors, leaving 12 microtextures that were analyzed by every author in the modern dataset. The microtextures in the "all-textures" ordination were arc-shaped steps, conchoidal fractures, linear steps, sharp angular features, subparallel linear fractures, edge rounding, v-shaped percussion cracks, curved grooves, precipitated features, low relief, medium relief, and high relief (Table S1). The "mechanical" ordination used 11 of the 12 microtextures in the "all-textures" ordination. The mechanical ordination excludes precipitated features and uses microtextures only created via mechanical processes.

The new PCA axes for each set of microtextures are shown in three biplots: A) PC1 vs. PC2, B) PC1 vs. PC3, and C) PC2 vs. PC3. In each biplot, 95% confidence ellipses centered at the mean were calculated for each modern transport mode using the methods of Schelp (2019). The broken-stick criterion (Frontier 1976; Jackson 1993; Legendre and Legendre 1998; Peres-

Neto et al. 2003) was used to determine the significance of the microtextural loadings in each ordination.

## RESULTS

### *Bråvika Member Field Observations*

Field observations of the Bråvika Member in Buldrevågen (79°59’29”N, 17°31’20”E), Geerabukta (79°38’06”N, 17°43’48”E), and Gimleodden (79°48’19”N, 18°24’04”E) show evidence of bedforms with 5-10 m wavelength and 1-3 m amplitude (Fig. 4A–C), trough cross-bedding (Fig. 4B–C), adhesion ripples (Fig. 4D–E), pinstripe lamination (at 9 m in Fig. 2C; Fig. 4F), and grains that are frosted, well-rounded, and well-sorted (Fig. 4G). At the Gimleodden site, there is also evidence of soft sediment deformation in the Bråvika Member at the contact with the Wilsonbreen Formation (Fig. 4I). At the Buldrevågen site, the Bråvika Member hosts sandstone intraclasts with diffuse boundaries and no obvious cements at 22 m above the base of the Bråvika Member (Figs. 2C, 4H, J–K), as well as pebbly sandstone intraclast conglomerates at 18 m and 22 m (7 m and 3 m below the Wilsonbreen Formation contact, respectively; Figs. 2C, 4J–K). The pebbly sandstone intraclast conglomerate is similar in color to the overlying Wilsonbreen Formation (Fig. 4L). The microtextural samples analyzed in this study from Buldrevågen were collected at 12 m and 22 m.

### *Microtextural Dataset Description*

This microtextural dataset is composed of 116 data points from modern and ancient aeolian, fluvial, and glacial settings. 92 of these data points come from modern settings and 24 come from ancient settings. The data are compiled from 11 studies: this study (9% of the total datapoints), Smith et al. (2018) (22%), Kalińska-Nartiša et al. (2017) (4%), Nartišs and Kalińska-Nartiša (2017) (2%), Sweet and Brannan (2016) (34%), Stevic (2015) (2%), Deane (2010) (8%), Sweet and Soreghan (2010) (3%), Mahaney et al. (2001) (3%), Mahaney et al. (1996) (9%), and Mahaney and Kalm (1995) (4%). Each data point in this analysis—with the exception of data points from Sweet and Soreghan (2010), Mahaney et al. (2001), and Mahaney and Kalm (1995)—represents one sample of *N* grains. The data points from Sweet and Soreghan (2010), Mahaney et al. (2001), and Mahaney and Kalm (1995) are the published averages of larger sets of unavailable raw data from each study. The data points are hereby referred to as samples.

Within the modern samples, 10% of the samples are aeolian, 45% are fluvial, and 45% are glacial. 60% of the modern aeolian samples come from periglacial settings and 73% of the modern fluvial samples come from glaciofluvial settings. All of the modern glacial samples come from active glacial environments. Within the ancient samples, 92% are constrained to particular depositional environments: 8% of the samples are aeolian, 21% are fluvial, and 63% are glacial. The remaining 8% of the ancient samples are from the Cryogenian Bråvika Member, and determining their depositional setting is a goal of this study.

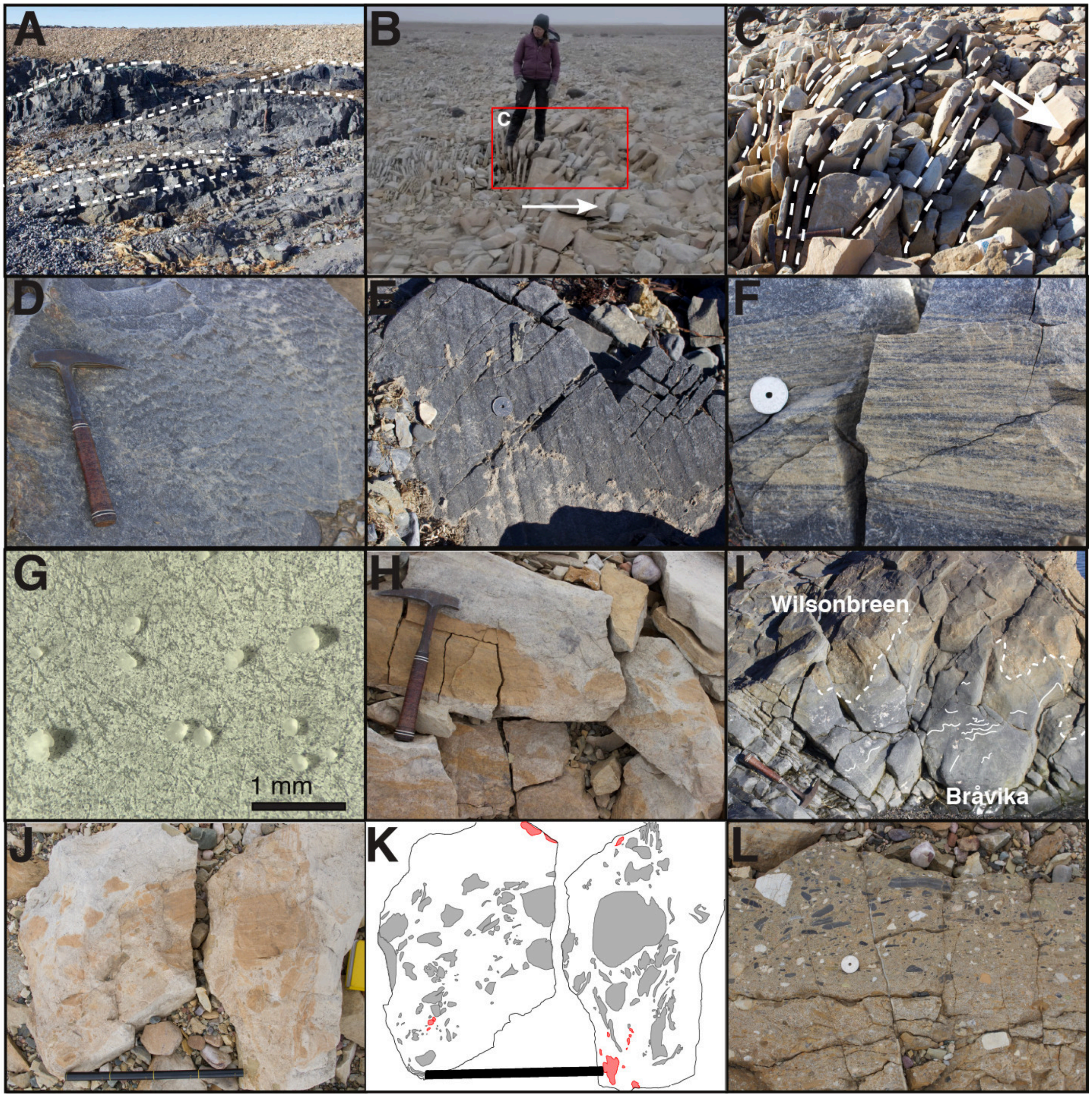


**Figure 4.** Field observations of the Bråvika Member and related units. All field photographs are of the Bråvika Member and are credited to K.D. Bergmann unless otherwise noted. A) Annotated photograph of large-scale bedforms exposed at Gimleodden. Dashed lines trace bedding surfaces. Hammer for scale. B) Photograph of frost-shattered trough crossbedding at 12 m in Buldrevågen (Fig. 2C), where the fracture planes are bedding surfaces. Arrow points upsection. The box highlights the location of C) (Photo credit: A.B. Jost). C) Annotated close-up of trough crossbedding. The dashed lines trace bedding surfaces and the arrow points upsection. D) Adhesion ripples on a bedding plane at Geerabukta. E) Potential adhesion ripples on a bedding plane at Gimleodden. F) Pinstripe lamination at Geerabukta. G) Photomicrograph of frosted grains from the Bråvika Member at Buldrevågen after dissolution of the dolomite cement with acid (Photo credit: J.N. Reahl). H) Close-up of sand intraclasts with diffuse edges at Buldrevågen. I) Soft sediment deformation in the upper Bråvika Member under the Wilsonbreen tillite at Gimleodden, consistent with deformation of unlithified Bråvika sand by overriding ice.

Some illustrative ductilely deformed sediments and intraclasts are noted with arrowheads. Dashed line marks the diffuse contact between the two units and solid lines trace contorted, folded beds within the Bråvika Member. Hammer for scale. J) Sandstone intraclasts with diffuse boundaries and greenish tan, pebbly, coarse sandstone intraclasts at 22 m in Buldrevågen (Fig. 2C). Bar is 40 cm long. K) Line drawing of J at the same scale; sandstone intraclasts are shaded gray, and greenish tan pebbly, coarse sandstone intraclasts are shaded red. L) The Wilsonbreen Formation at Buldrevågen, pictured here, has a greenish tan pebbly sandstone matrix.

*Probability of Occurrence*

**Modern Samples.**—— Modern aeolian samples are the most likely to have edge rounding (0.90 avg.), precipitated features (0.59 avg.), and low relief (0.31 avg.) compared to modern fluvial and glacial samples, which in turn are more likely to have high relief (0.40 fluvial avg.; 0.36 glacial avg.) and subparallel linear fractures (0.63 fluvial avg.; 0.50 glacial avg.) (Fig. 5). These transport modes also share similar probabilities of occurrence for some features. Glacial and aeolian samples share similar probabilities of curved grooves (0.33 glacial avg., 0.27 aeolian avg.) compared to fluvial samples. Fluvial and aeolian samples also share similar probabilities of v-shaped percussion cracks (0.45 fluvial avg., 0.48 aeolian avg.) compared to glacial samples. The probability of occurrence of arc-shaped steps, conchoidal fractures, linear steps, sharp angular features, and medium relief are not substantially different between the three transport modes.

Study-specific variations in microtextural probabilities occur within each transport mode. In the aeolian transport mode, samples from Stevic (2015) (samples 20–21; Table 1) are more likely to have curved grooves (0.80–0.93) compared to most other aeolian samples in the dataset (0.13–0.19). The fluvial grains from Sweet and Brannan (2016) (sample 19) are more likely to have v-shaped percussion cracks (0.82) compared to the remaining fluvial samples from Smith et al. (2018) (0.15–0.40). Glacial grains from this study (samples 6–9) and Kalińska-Nartiša et al. (2017) (sample 17) have the highest probabilities of edge rounding (0.29–0.91) and precipitated features (0.55–0.88) compared to the remaining glacial samples. The glacial grains from Kalińska-Nartiša et al. (2017) are also the most likely to have low relief (0.68).

**Ancient Samples.** —— Both samples from the Cryogenian Bråvika Member (samples 32–33; Table 2) have particularly high probabilities of edge rounding (1.00), precipitated features (1.00), and upturned plates (0.85–0.97; Fig. 6). Pleistocene aeolian sand samples from Nartišs and Kalińska-Nartiša (2017) (samples 34–35) have high abundances of edge rounding, dissolution etching, and precipitated features (all categorized as “abundant”; >0.75 probability of occurrence). The fluvial samples associated with the Fountain Formation in Colorado (samples 45–47; Sweet and Soreghan 2010) are more likely to have edge rounding (0.49–0.72) and low relief (0.26–0.45) compared to the modern fluvial average. Grains from the Pleistocene glaciofluvial sand samples (sample 49) and middle Devonian Arküla Stage fluvial sand samples (sample 48) from Estonia (Mahaney et al. 2001) are more likely to have edge rounding (0.56–0.64), v-shaped percussion cracks (0.53–0.61), and low relief (0.35–0.59) compared to grains from the modern fluvial average. All of the ancient fluvial samples have lower probabilities of arc-shaped steps (0.00–0.23), conchoidal fractures (0.06–0.39), linear steps (0.00–0.26),

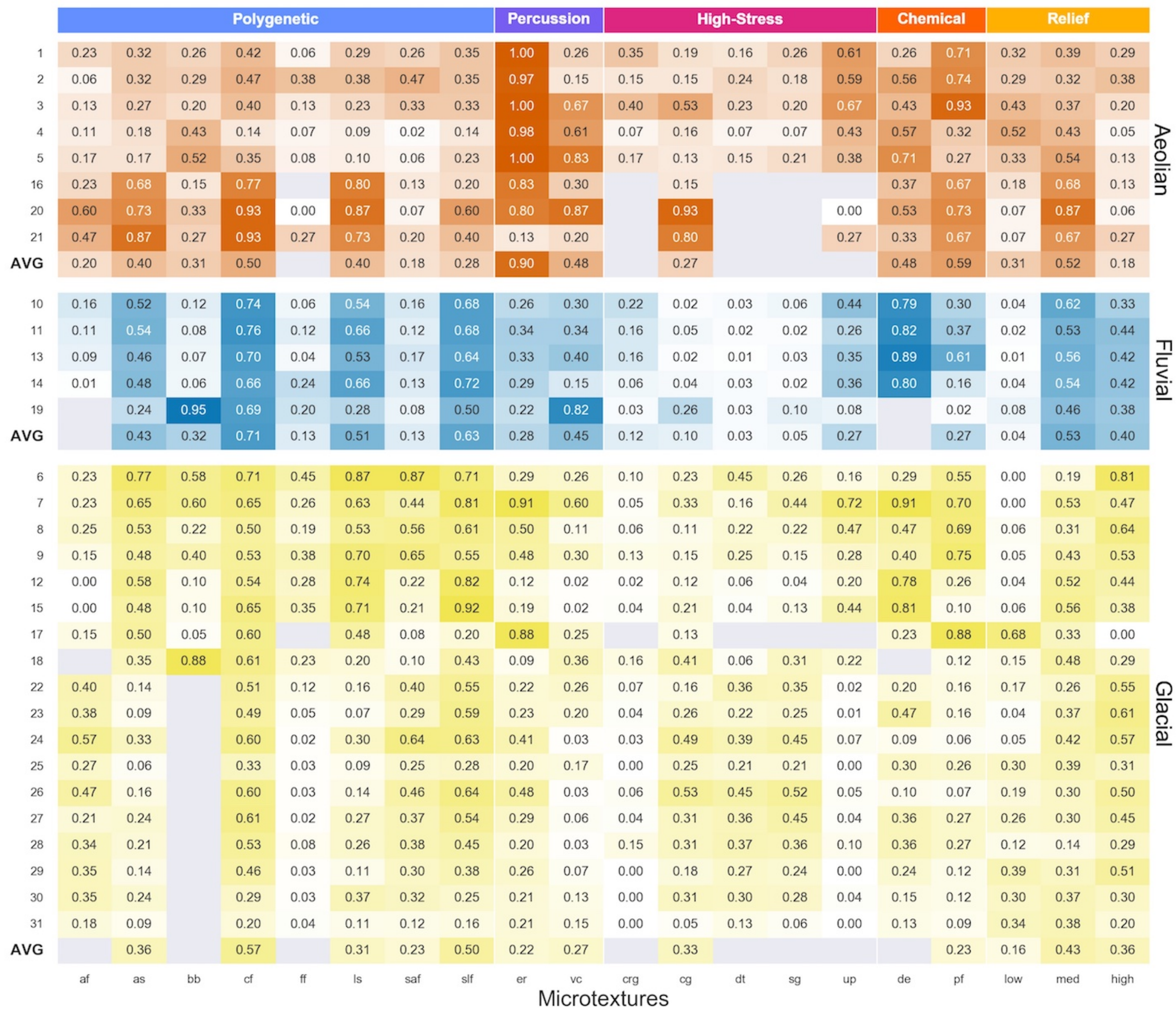


**Figure 5.** Heatmap of the microtextural probabilities of occurrence from 0 to 1 for each modern sample group used in the analysis. Samples are binned into aeolian, fluvial, and glacial transport modes. Refer to Table 1 for sample group numbers and descriptions. Data are averaged for sample groups that contain more than one sample (S > 1). Refer to Figure 3A and B for microtextural abbreviations. The average of each transport mode for the modern samples (AVG) is at the bottom of each bin. All averages were calculated using Equation 1. Microtextures that were not analyzed within a study are grayed out.

subparallel linear fractures (0.08–0.35), upturned plates (0.00–0.04), and high relief (0.05–0.18) compared to the modern fluvial average. Grains from the Pleistocene tills in Costa Rica and the Dominican Republic (samples 36-44; Deane 2010) are more likely to have subparallel linear fractures (0.86-0.96) and medium relief (0.60-0.76) compared to the modern glacial average. The Pleistocene tills from Mahaney et al. (2001) (sample 50) and Mahaney and Kalm (1995) (samples 51-55) are broadly comparable to the modern glacial average.

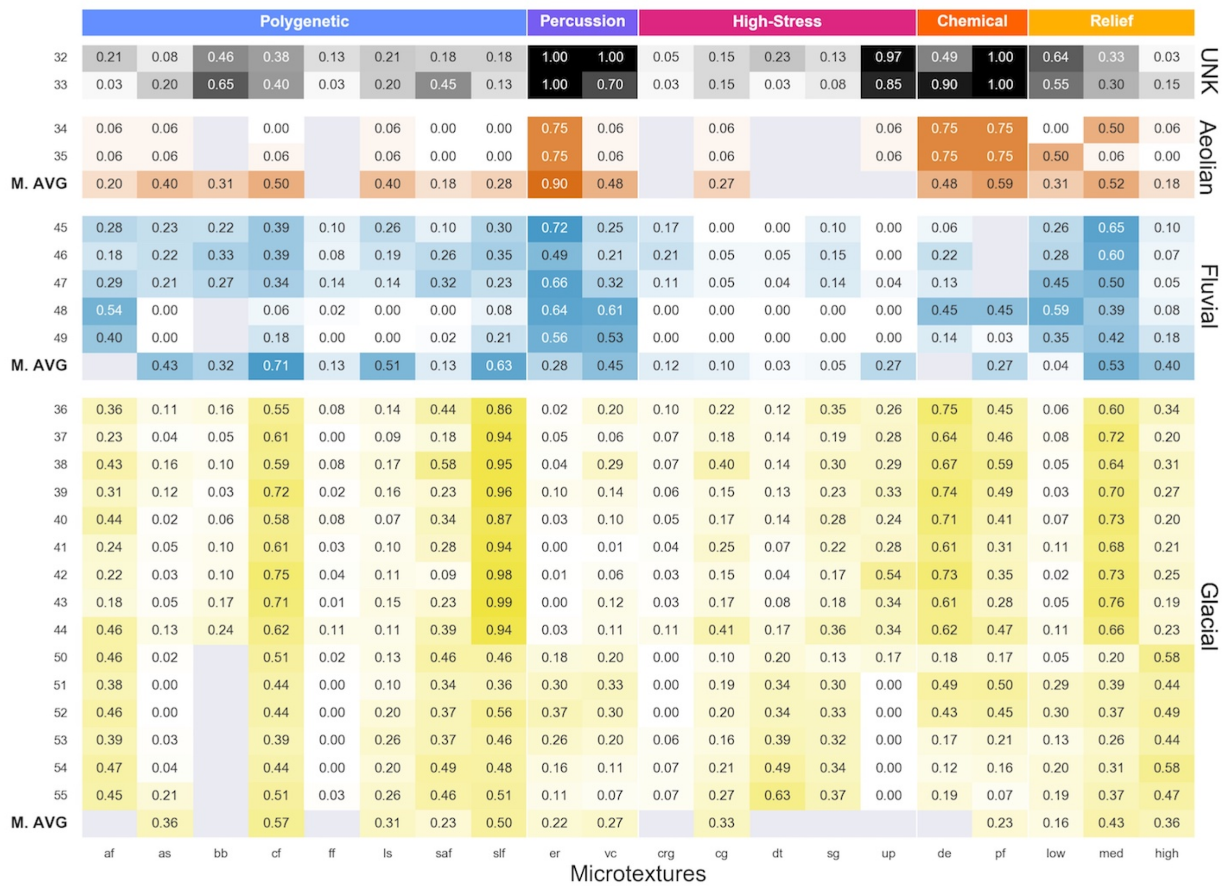


**Figure 6.** Heatmap of the microtextural probabilities of occurrence from 0 to 1 for each ancient sample group used in the analysis. Samples are binned into "unknown" (UNK; Bråvika Member), aeolian, fluvial, and glacial transport modes. Refer to Table 2 for sample group numbers and descriptions. Data are averaged for sample groups that contain more than one sample (S > 1). Refer to Figure 3A and B for microtextural abbreviations. The average of each transport mode for the modern samples (M. AVG) from Figure 5 is at the bottom of each bin. All averages were calculated using Equation 1. Microtextures that were not analyzed within a study are grayed out.

### *Principal Component Analysis*

**All Textures Analyzed by All Authors.** —– Within the all-textures PCA ordination, the PC1, PC2, and PC3 axes capture about 66% of the variance in the modern dataset (27.01%, 21.33%, and 17.43%, respectively; Table 3). Along the PC1 axis (Figs. 7-A1, 8-A1 and B1), the aeolian, fluvial, and glacial samples are distributed along both sides of the axis with no clear separation: the aeolian samples have an interquartile range (IQR) between -2.6 and 1.3; the fluvial samples have an IQR between -2.0 and 0.4; and the glacial samples have an IQR between 0.2 and 1.9 (Table S3). However, the samples are distinctly separated by study along PC1 (Figs. 8-A1 and B1, S4-A1): the samples from Smith et al. (2018) and Stevic (2015) have IQRs distributed between -2.7 and -1.8 on PC1; and the samples from Sweet and Brannan (2016) and Mahaney et al. (1996) have IQRs distributed between 0.4 and 2.1 (Table S4). The samples from

**Table 3.** Percentage variance of each principal component axis for each PCA ordination.

| PCA Ordination | Axis | Individual [%] | Cumulative [%] |
|---|---|---|---|
| All Microtextures | PC1 | 27.01 | 27.01 |
| | PC2 | 21.33 | 48.34 |
| | PC3 | 17.43 | 65.77 |
| Mechanical Microtextures | PC1 | 28.37 | 28.37 |
| | PC2 | 20.04 | 48.41 |
| | PC3 | 17.32 | 65.73 |

**Table 4.** Ranked loadings and squared loadings of microtextures from the all-textures PCA ordination (Fig. 8). Refer to Figure 3A and B for microtexture abbreviations. The microtextures in bold have squared loadings that are greater than the expected value of their associated principal component according to the broken-stick criterion (Frontier 1976; Jackson 1993; Legendre and Legendre 1998; Peres-Neto et al. 2003).

| PC1 | | | PC2 | | | PC3 | | |
|---|---|---|---|---|---|---|---|---|
| Expected PC Value: | | 0.259 | Expected PC Value: | | 0.175 | Expected PC Value: | | 0.134 |
| Microtexture | Loading | Loading$^2$ | Microtexture | Loading | Loading$^2$ | Microtexture | Loading | Loading$^2$ |
| low | 0.286 | 0.082 | **low** | **0.457** | **0.209** | **saf** | **0.592** | **0.351** |
| cg | 0.239 | 0.057 | **er** | **0.455** | **0.207** | **high** | **0.411** | **0.169** |
| vc | 0.141 | 0.020 | **pf** | **0.432** | **0.186** | pf | 0.153 | 0.023 |
| high | -0.104 | 0.011 | as | 0.139 | 0.019 | slf | 0.135 | 0.018 |
| saf | -0.114 | 0.013 | ls | 0.112 | 0.013 | er | 0.126 | 0.016 |
| er | -0.128 | 0.017 | med | 0.090 | 0.008 | low | 0.089 | 0.008 |
| pf | -0.272 | 0.074 | saf | 0.018 | 0.000 | ls | 0.019 | 0.000 |
| med | -0.300 | 0.090 | cg | -0.028 | 0.001 | as | -0.055 | 0.003 |
| cf | -0.324 | 0.105 | vc | -0.153 | 0.023 | cg | -0.071 | 0.005 |
| slf | -0.335 | 0.112 | cf | -0.168 | 0.028 | cf | -0.279 | 0.078 |
| as | -0.425 | 0.181 | slf | -0.350 | 0.123 | vc | -0.312 | 0.097 |
| ls | -0.489 | 0.239 | **high** | **-0.427** | **0.182** | **med** | **-0.482** | **0.232** |

this study and Kalińska-Nartiša et al. (2017) are distributed on both sides of PC1, where the samples from this study have an IQR between -2.1 and 1.6 and the Kalińska-Nartiša et al. (2017) samples have an IQR between -2.7 and -0.3. The sample separation along PC1 is predominantly driven by the abundance of linear steps and arc-shaped steps, which have the largest (-0.489) and second largest (-0.425) negative loadings along PC1 (Table 4; Fig. 8-A2 and B2). However, neither of these loadings are strongly associated with PC1 according to the broken-stick criterion (Table 4).

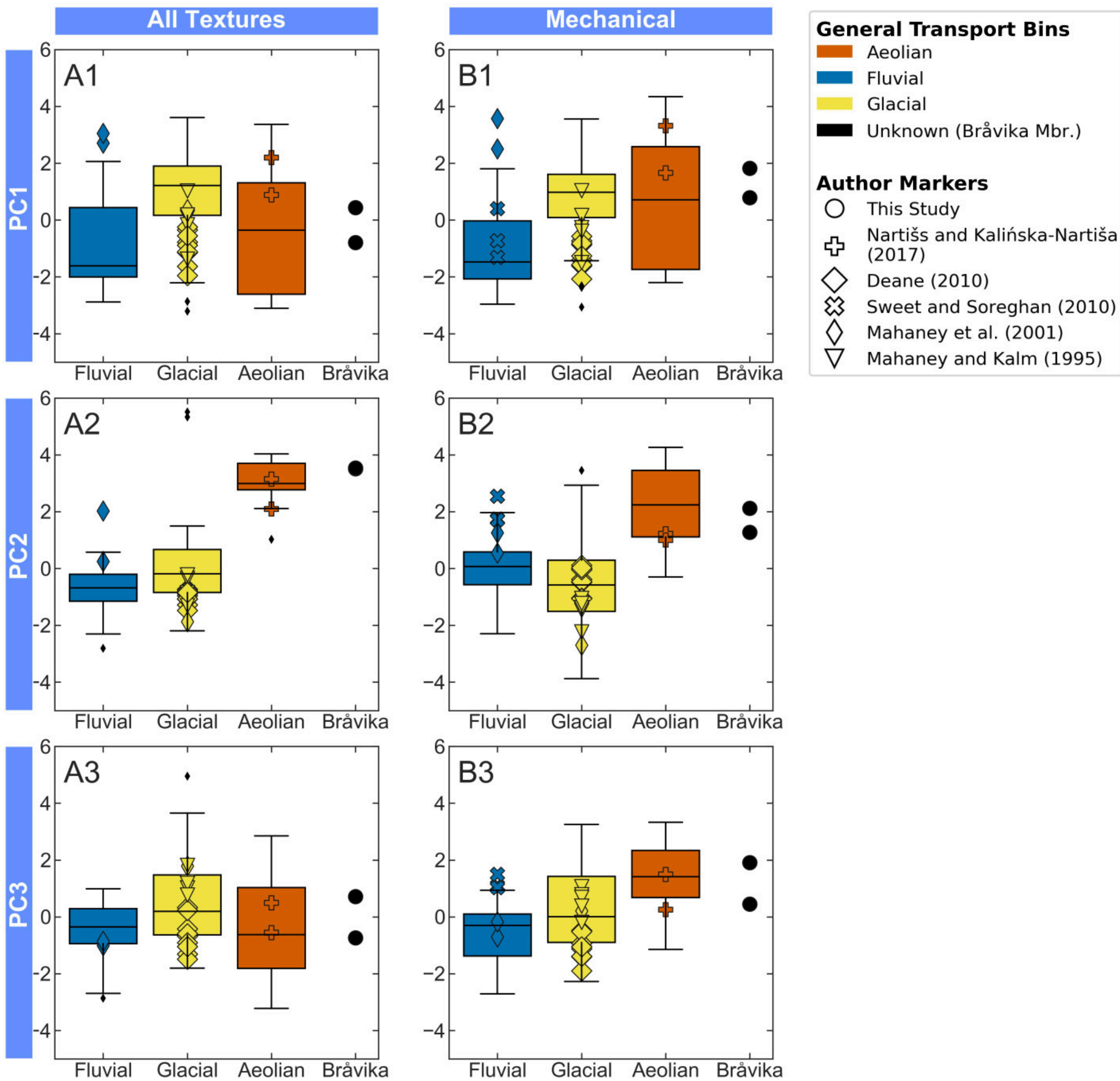


**Figure 7.** Boxplots of the modern aeolian, fluvial, and glacial samples (box and whiskers) in the all-textures PCA ordination (column A) and the mechanical PCA ordination (column B). Each column represents a principal component axis in each ordination: PC1 (row 1), PC2 (row 2), and PC3 (row 3). The small black diamonds represent modern outliers for each transport mode. The ancient samples are plotted as individual points over the boxplots.

Along the PC2 axis (Figs. 7-A2, 8-A1 and C1; Table S3), the aeolian samples have an IQR between 2.8 and 3.7 and the modern glacial and fluvial samples have IQRs distributed between -1.2 to 0.7. This separation between aeolian and fluvial/glacial samples along PC2 is driven by low relief, edge rounding, and precipitated features in the positive direction (loadings of 0.457, 0.455, and 0.432) and high relief in the negative direction (-0.427), which are all associated with PC2 according to the broken-stick criterion (Table 4; Fig. 8-A2 and C2).

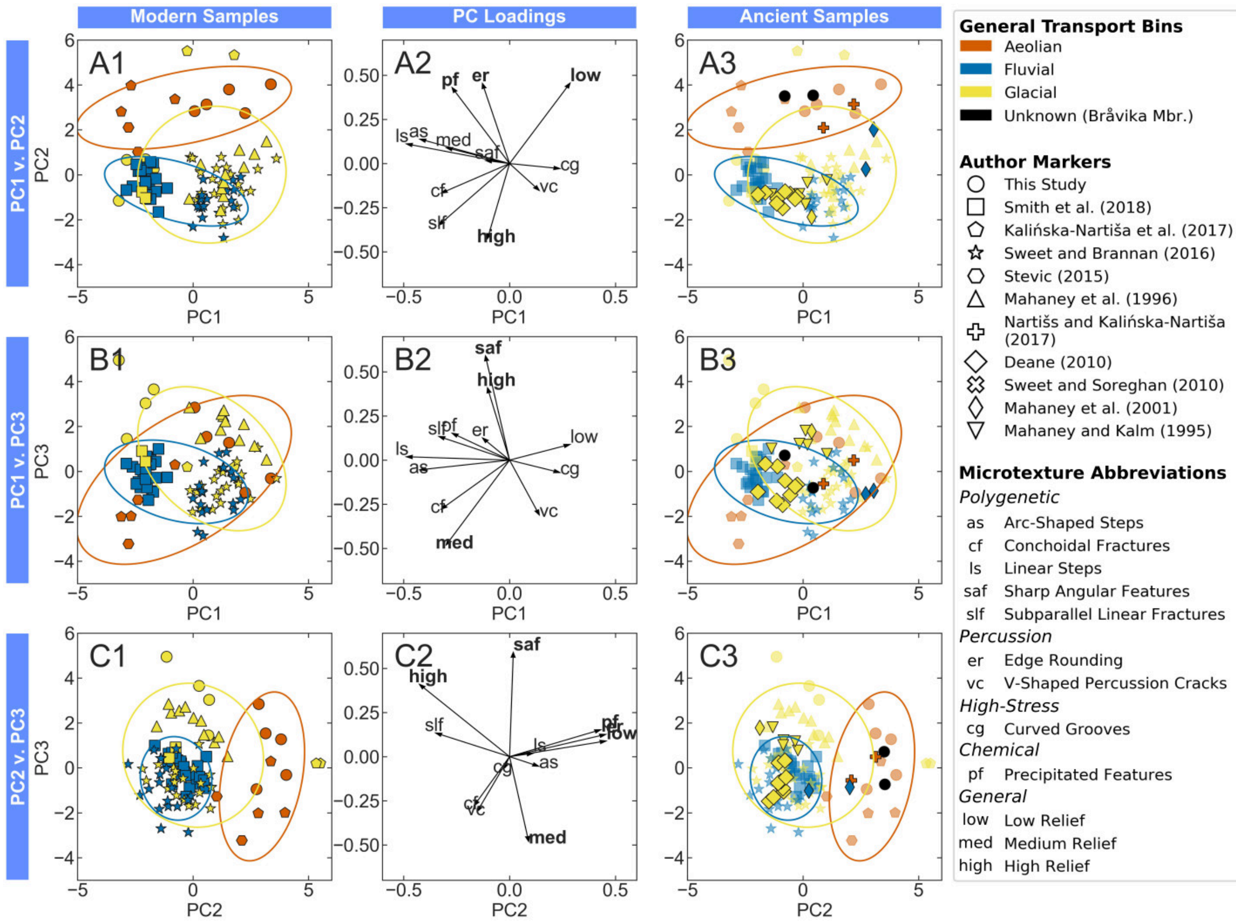


**Figure 8.** All-textures PCA ordination using all 12 microtextures analyzed by all studies. Each row is a biplot in A) PC1-PC2 space; B) PC1-PC3 space; and C) PC2-PC3 space. Column 1 plots the modern sample data within each space (this study through Mahaney et al. 1996), Column 2 plots the microtextural loadings, and Column 3 plots the ancient sample data (this study, Nartišs and Kalińska-Nartiša 2017 through Mahaney and Kalm 1995) over the existing modern reference frame. Refer to Table 4 for the loadings in Column 2. Microtextures with significant loadings in Column 2 are in bold. The ellipses are 95% confidence intervals of each modern transport mode that are centered at the mean of the transport mode in each coordinate space. The ellipses are calculated using the methods of Schelp (2019).

Along the PC3 axis, the three transport modes are distributed along both sides of the axis with no clear separation, similar to the distribution along PC1: the aeolian samples have an IQR between -1.8 and 1.0, the fluvial samples have an IQR between -0.9 and 0.3, and the glacial samples have an IQR between -0.6 and 1.5 (Figs. 7-A3, 8-B1 and C1; Table S3). However, unlike the distribution along PC1, the samples are not as distinctly separated by study (Fig. S4-A3). The significant microtextures along PC3 are sharp angular features and high relief in the positive direction (0.592 and 0.411), and medium relief in the negative direction (-0.482; Table 4; Fig. 8-B2 and C2). All of these microtextures are associated with PC3 according to the broken-stick criterion (Table 4).

Along each principal component axis in the all-textures ordination (Fig. 7 column A), at least 89% of the ancient aeolian, fluvial, and glacial samples plot within the upper and lower adjacent values of their modern counterparts: 89% on PC1 (A1), 95% on PC2 (A2), and 100% on PC3 (A3). In each biplot (Fig. 8 column 3), at least 74% of these ancient samples plot within the 95% confidence ellipses of their modern counterparts: 89% in the PC1-PC2 biplot (A3), 74% in the PC1-PC3 biplot (B3), and 95% in the PC2-PC3 biplot (C3). The median of the percent agreement between ancient samples and their modern counterparts for the all-textures ordination is 92%. Sensitivity tests demonstrate that the aeolian Nartišs and Kalińska-Nartiša (2017) samples plot within the boundaries of the modern aeolian samples regardless of the assigned values for each abundance bin (Fig. S2). Because the fluvial Pennsylvanian-Lower Permian Fountain Formation samples from Sweet and Soreghan (2010) do not count precipitated features, they were not included in this ordination.

The 92% median agreement between the modern and ancient samples from known environments in the all-textures ordination demonstrates that modern samples provide a valid framework for interpreting the fingerprint of depositional environments in ancient samples. In this ordination, the two Bråvika Member samples with ambiguous depositional histories consistently plot within the upper and lower adjacent values of the modern aeolian samples in each principal component axis (Fig. 7 column A) and the 95% confidence ellipses of the modern aeolian samples in each biplot (Fig. 8 column 3). This placement suggests that the Bråvika Member samples analyzed in this study have an aeolian origin.

**Mechanical Textures Analyzed by All Authors. ——** Within the mechanical PCA ordination, the PC1, PC2, and PC3 axes also capture about 66% of the variance in the modern dataset (28.37%, 20.04%, 17.32%, respectively; Table 3). As in the previous PCA ordination, the aeolian, fluvial, and glacial samples are distributed along both sides of the PC1 axis with no clear separation (Figs. 7-B1, 9; Table S3). Instead, the samples are separated by study, where the Smith et al. (2018) and Stevic (2015) samples have IQRs distributed between -2.2 and -1.8 and are distinctly separated from the remaining authors (Fig. S4; Table S4). This sample separation along PC1 is driven by the abundance of linear steps (-0.449), subparallel linear fractures (-0.413), arc-shaped steps (-0.381), and conchoidal fractures (-0.376) (Table 5; Fig. 9-A2 and B2). None of these features are associated with PC1 according to the broken-stick criterion (Table 5).

Along the PC2 axis (Fig. 9-A1 and C1), the modern aeolian samples are still separated from the fluvial and glacial samples. However, compared to the all-textures PCA ordination, the aeolian samples are not as separated from the fluvial and glacial samples: the spacing between the aeolian lower quartile and the fluvial/glacial upper quartile in the mechanical ordination is only 0.5 compared to a spacing of 2.1 in the all-textures ordination (Fig. 7-B2). This separation is driven by medium relief (0.460) in the positive direction and high relief (-0.586) in the negative direction. Both features are significantly associated with the PC2 axis according to the broken-stick criterion (Table 5; Fig. 9-A2 and C2).

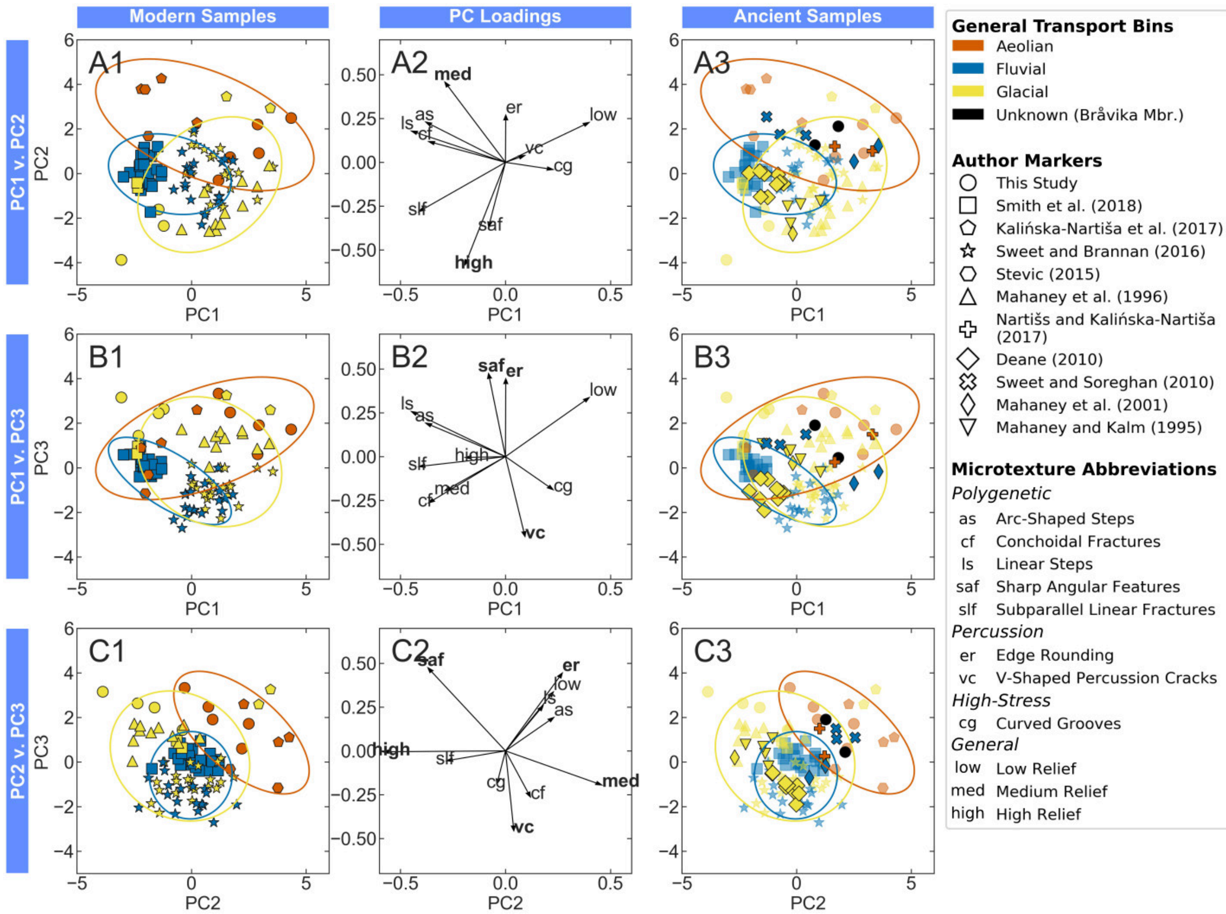


**Figure 9.** Mechanical PCA ordination using all 11 mechanical microtextures analyzed by all studies. These plots are in the same format as shown in Figure 8: each row is a biplot in A) PC1-PC2 space; B) PC1-PC3 space; and C) PC2-PC3 space. Column 1 plots the modern sample data within each space (this study through Mahaney et al. 1996), Column 2 plots the microtextural loadings, and Column 3 plots the ancient sample data (this study, Nartišs and Kalińska-Nartiša 2017 through Mahaney and Kalm 1995) over the existing modern reference frame. Refer to Table 5 for the loadings in Column 2. Microtextures with significant loadings in Column 2 are in bold. The ellipses are 95% confidence intervals of each modern transport mode that are centered at the mean of the transport mode in each coordinate space. The ellipses are calculated using the methods of Schelp (2019).

As in the previous ordination, the three transport modes along PC3 are distributed along both sides of the axis with no clear separation, similar to the distribution along PC1 (Figs. 7-B3, 9-B1 and C1). The samples are also not distinctly separated by study (Fig. S4-B3). This separation is driven by sharp angular features (0.476) and edge rounding (0.446) in the positive direction and v-shaped percussion cracks (-0.458) in the negative direction. Each of these microtextures are significant according to the broken-stick criterion (Table 5; Fig. 9-B2 and C2).

In the mechanical ordination, the ancient aeolian, fluvial, and glacial samples consistently plot alongside their modern counterparts. However, the percent agreement between the ancient and modern samples is overall lower for the mechanical ordination than the all-textures

**Table 5.** Ranked loadings and squared loadings of microtextures from the mechanical PCA ordination (Fig. 9). Refer to Figure 3A and B for microtexture abbreviations. The microtextures in bold have squared loadings that are greater than the expected value of their associated principal component according to the broken-stick criterion (Frontier 1976; Jackson 1993; Legendre and Legendre 1998; Peres-Neto et al. 2003).

| PC1 | | | PC2 | | | PC3 | | |
|---|---|---|---|---|---|---|---|---|
| Expected PC Value: | | 0.275 | Expected PC Value: | | 0.184 | Expected PC Value: | | 0.138 |
| Microtexture | Loading | $Loading^2$ | Microtexture | Loading | $Loading^2$ | Microtexture | Loading | $Loading^2$ |
| low | 0.400 | 0.160 | **med** | **0.460** | **0.211** | **saf** | **0.476** | **0.226** |
| cg | 0.228 | 0.052 | er | 0.271 | 0.074 | **er** | **0.446** | **0.199** |
| vc | 0.093 | 0.009 | as | 0.231 | 0.053 | low | 0.338 | 0.114 |
| er | 0.001 | 0.000 | low | 0.229 | 0.052 | ls | 0.258 | 0.067 |
| saf | -0.081 | 0.007 | ls | 0.180 | 0.032 | as | 0.192 | 0.037 |
| high | -0.193 | 0.037 | cf | 0.119 | 0.014 | high | -0.005 | 0.000 |
| med | -0.289 | 0.084 | vc | 0.040 | 0.002 | slf | -0.057 | 0.003 |
| cf | -0.367 | 0.135 | cg | -0.041 | 0.002 | cg | -0.190 | 0.036 |
| as | -0.381 | 0.145 | slf | -0.282 | 0.079 | med | -0.195 | 0.038 |
| slf | -0.413 | 0.171 | saf | -0.370 | 0.137 | cf | -0.265 | 0.070 |
| ls | -0.449 | 0.202 | **high** | **-0.586** | **0.343** | **vc** | **-0.458** | **0.209** |

ordination. Along each principal component axis in the mechanical ordination (Fig. 7 column B), at least 86% of the ancient aeolian, fluvial, and glacial samples plot within the upper and lower adjacent values of their modern counterparts: 91% on PC1 (B1), 95% on PC2 (B2), and 86% on PC3 (B3). In each biplot (Fig. 9 column 3), at least 64% of these ancient samples plot within the 95% confidence ellipses of their modern counterparts: 73% in the PC1-PC2 biplot (A3), 64% in the PC1-PC3 biplot (B3), and 86% in the PC2-PC3 biplot (C3). The median of the percent agreement between ancient samples and their modern counterparts for the mechanical ordination is 86%, which is lower than the all-textures ordination's median value of 92%. As in the previous ordination, sensitivity tests demonstrate that the aeolian Nartišs and Kalińska-Nartiša (2017) samples plot within the boundaries of the modern aeolian samples regardless of the assigned values for each abundance bin (Fig. S3). The fluvial Pennsylvanian-Lower Permian Fountain Formation samples from Sweet and Soreghan (2010) do not consistently plot near the fluvial samples; instead, they plot closer to the other aeolian samples.

The 86% median agreement between the modern and ancient samples from known environments in the mechanical ordination demonstrates that modern samples provide a valid framework for interpreting the fingerprint of depositional environments in ancient samples. As in the previous ordination, the two Bråvika Member samples with ambiguous depositional histories consistently plot within the upper and lower adjacent values of the modern aeolian samples in each principal component axis (Fig. 7 column B) and the 95% confidence ellipses of the modern aeolian samples in each biplot (Fig. 9 column 3). This placement suggests that the Bråvika Member samples analyzed in this study have an aeolian origin.

## DISCUSSION

### *Interpreting the PCA Ordinations*

In both ordinations, PC1 separates the modern samples by author and accounts for the most variance in the dataset (Table 3), indicating that author-specific microtextural variance is the largest individual source of variance in the modern dataset. This result is consistent with the observation that SEM operator variance exerts significant influence on the probabilities of occurrence of individual microtextures (Culver et al. 1983). However, as Culver et al. (1983) observed using canonical variate analysis, author variance is overall negligible in determining a sample's depositional environment: the combined variance of PC2 and PC3 accounts for over a third of the variance in the modern dataset (Table 3) and biplots of these axes separate the samples into aeolian and fluvial/glacial transport modes in both ordinations (Figs. 8, 9). Therefore, PCA can be used to distinguish transport modes from each other regardless of author, as well as identify the most significant microtextures separating these transport modes in this dataset.

### *Which Microtextures Distinguish Transport Modes?*

Aeolian sediment is defined by high probabilities of low relief, edge rounding, and precipitated features, and fluvial and glacial sediment are defined by high probabilities of high relief and subparallel linear fractures. The modern (Fig. 5) and ancient (Fig. 6) heatmaps show that aeolian samples have the highest probabilities of low relief, edge rounding, and precipitated features, and fluvial and glacial samples have the highest probabilities of high relief and subparallel linear fractures. PC2 in the all-textures ordination (Fig. 8) also separates the aeolian samples from the fluvial and glacial samples using low relief, edge rounding, and precipitated features in the positive (aeolian) direction and high relief in the negative (fluvial/glacial) direction (Table 4). These findings are consistent with previous observations of these microtextures: low relief, edge rounding, and precipitated features have all previously been associated with windblown sediment (Nieter and Krinsley 1976; Lindé and Mycielska-Dowgiałło 1980; Krinsley and Trusty 1985; Mahaney 2002; Vos et al. 2014); high relief can occur on both fluvial and glacial sediments (Mahaney 2002; Vos et al. 2014); and subparallel linear fractures are often associated with glacial and glaciofluvial settings, the latter of which makes up 73% of the modern fluvial samples in this study (Mahaney and Kalm 2000; Deane 2010; Immonen 2013; Vos et al. 2014; Woronko 2016). Although the PC2 axis in the mechanical ordination creates this same separation using medium relief in the positive (aeolian) direction and high relief in the negative (fluvial/glacial) direction, medium relief can occur in all transport modes (Vos et al. 2014), suggesting that the aeolian samples' low probability of high relief separates them from the fluvial and glacial samples along PC2.

Although fluvial and glacial samples are microtexturally distinct from aeolian samples, it is difficult to disambiguate the fluvial and glacial transport modes from each other in this dataset. Features that are typically associated with glacial environments, such as arc-shaped steps, conchoidal fractures, linear steps, and sharp angular features (Mahaney and Kalm 2000; Mahaney 2002; Immonen 2013; Woronko 2016), had comparable probabilities across all three modern transport modes, indicating that these features are not exclusively associated with glacial environments (Fig. 5). Smith et al. (2018) also observed that arc-shaped steps and linear steps may not be indicators of glacial transport. These results are consistent with Sweet and Soreghan's (2010) classification of these features as *polygenetic* features that are formed through a variety of transport processes. Subparallel linear fractures are also associated with glacial and glaciofluvial settings (Mahaney and Kalm 2000; Deane 2010; Immonen 2013; Vos et al. 2014; Woronko 2016), but the modern fluvial average for subparallel linear fractures is higher than the glacial average. Although glaciofluvial samples make up 73% of the modern fluvial samples, the non-glacial fluvial samples (samples 10 and 13; Fig. 5) have similar probabilities of subparallel linear fractures compared to glaciofluvial samples (samples 11, 14, and 19), suggesting that subparallel linear fractures may not be an exclusively glacial feature. These results suggest that fluvial and glacial samples are microtexturally similar, and more studies comparing the microtextural features of non-glacial fluvial, glaciofluvial, and glacial samples are needed to understand the differences between these transport environments.

This dataset and the PCA ordinations highlight the importance of precipitated features as a primary indicator of transport instead of an exclusive product of diagenesis. If precipitated features were only an indicator of post-depositional diagenesis, then the probability of precipitated features should increase with age. However, all of the modern samples have some probability of having precipitated features—particularly the aeolian samples—and the ancient samples do not show a consistent increase in the probability of chemical features as the sediment age increases (Figs. 5, 6). Both of these observations point to precipitated features being a primary microtextural feature. In addition to the microtextural data, the median percent agreement between the modern and ancient samples is higher for the all-textures PCA ordination (92%) compared to the median value for the mechanical PCA ordination (86%). This difference indicates that the presence or absence of precipitated features in an ordination significantly affects an ordination's ability to accurately match ancient aeolian, fluvial, and glacial samples with their modern counterparts. Although Sweet and Soreghan (2010) suggested that precipitated features should not be counted because they can form via diagenesis and overprint a sample, our results indicate that these features can also be a primary feature and should not be discounted, even in situations where diagenesis is a concern.

Some microtextures often used in microtextural studies could not be included in these analyses: abraded features, breakage blocks, crescentic gouges, fracture faces, deep troughs, straight grooves, upturned plates, and dissolution etching. Many of these microtextures have been previously associated with certain transport environments. Breakage blocks, straight grooves, and fracture faces have been associated with glacial environments (Woronko 2016) and upturned plates and dissolution etching have been associated with aeolian environments (Margolis and Krinsley 1974; Mahaney 2002). For the purposes of comparing microtextural data from multiple studies, we were limited to using the most often used microtextures in the microtextural community. Moving forward, it would be helpful to establish a consistent minimum set of microtextures to be used in microtextural studies.

### *Test Case: The Cryogenian Bråvika Member*

We now shift our focus to using the microtextural data, PCA ordinations, and stratigraphic observations to constrain the depositional environment of the Cryogenian Bråvika Member from Buldrevågen, Svalbard. There are three prevailing hypotheses for what facies the Bråvika Member could represent: 1) a glaciofluvial outwash plain associated with the Wilsonbreen Formation (Halverson et al. 2004); 2) an aeolian facies associated with the glacial conditions of the Wilsonbreen Formation or the tropical equatorial conditions of the Elbobreen Formation (Halverson 2011); and 3) a tropical fluvial environment associated with the upper Elbobreen Formation (Hoffman et al. 2012). Our combined field observations and microtextural data suggest that the Bråvika Member includes aeolian deposition that may be time equivalent with the onset of the syn-glacial Marinoan Wilsonbreen Formation.

The microtextural evidence point to an aeolian origin for the Bråvika Member. Both samples from the Bråvika Member have particularly high occurrences of edge rounding, precipitated features, and low relief (samples 32 and 33; Fig. 6), which have all been previously associated with aeolian transport (Nieter and Krinsley 1976; Lindé and Mycielska-Dowgiałło 1980; Krinsley and Trusty 1985; Mahaney 2002; Vos et al. 2014). The Bråvika Member samples also have high probabilities of upturned plates, which have been associated with grain frosting (Margolis and Krinsley 1971). Compared to the modern and ancient aeolian, fluvial, and glacial samples, the Bråvika Member samples are most similar to the aeolian samples, sharing similar probabilities of low relief, edge rounding, and precipitated features (Fig. 6). These samples also consistently plot within the upper and lower adjacent values (Fig. 7) and 95% confidence ellipses (Figs. 8, 9) of the modern aeolian samples. Because the ancient aeolian, fluvial, and glacial samples are accurately matched with their modern counterparts 92% (all-textures) and 86% (mechanical) of the time when transformed into modern PCA space, both PCA ordinations are able to accurately plot samples with ambiguous depositional histories alongside their most likely modern microtextural analogs.

An aeolian interpretation for the microtextural data is consistent with field observations made in 2017 of the Bråvika Member in Buldrevågen, Geerabukta, and Gimleodden (Fig. 4). Bedforms with 5–10 m wavelengths and 1–3 m amplitudes at the Gimleodden (Fig. 4A) and Buldrevågen (Fig. 4B–C) sites are consistent with aeolian dunes in scale and style (Wilson 1972; Pye and Tsoar 2009). There is also evidence of adhesion ripples on bedding planes at the Geerabukta (Fig. 4D) and Gimleodden (Fig. 4E) sites. Adhesion ripples are formed when dry, windblown sand is blown onto a wet surface, and these features have been previously observed on ancient aeolian deposits (Kocurek and Fielder 1982). The presence of pinstripe lamination at the Buldrevågen (Fig. 2C) and Geerabukta (Fig. 4F) sites are a strong indicator for aeolian deposition (Fryberger and Schenk 1988). The high degree of grain rounding at this interval (Fig. 4G) is also characteristic of grains transported by aeolian processes (Folk 1980; Garzanti et al. 2015; Garzanti 2017); subaqueous transport does not typically produce such a high degree of grain rounding (Pettijohn 1957). The frosted grains within these samples (Fig. 4G) are also a strong indicator of aeolian transport (Pye and Tsoar 2009).

Field evidence also suggests that the aeolian strata of the Bråvika Member may be syn-depositional with the Marinoan pan-glaciation as opposed to the Cryogenian interglacial. The pebbly sandstone intraclast conglomerates' proximity to the contact with—and similar color and texture as—the Wilsonbreen Formation (Figs. 2C, 4J–L) suggest that they are sourced from this unit. These intraclasts' occurrences at 7 m and 3 m below the Wilsonbreen Formation contact (Fig. 2C) suggest that the Bråvika Member in Buldrevågen was syn-depositional with the Wilsonbreen Formation and the Marinoan pan-glaciation. The intraclasts with diffuse boundaries and no obvious cements at 22 m (Figs. 2C, 4A–C) are putative ice-cemented sand intraclasts. Ice-cemented intraclasts form when water within the pore space of unconsolidated sand freezes portions of sand into discrete clasts that can be transported and deformed into new orientations before the cementing ice melts. Sand intraclasts are routinely identified as ice-cemented in glaciogenic deposits (Browne and Naish 2003), and Runkel et al. (2010) has reported putative ice-cemented sand intraclasts preserved in rocks as old as the middle to late Cambrian. The putative ice-cemented intraclasts indicate that the Bråvika Member was at least unconsolidated during the Marinoan pan-glaciation, and the possible Wilsonbreen intraclasts' occurrence 3 m below the Wilsonbreen Formation contact (Fig. 2C) suggests that the Bråvika Member was syn-depositional with the Marinoan glaciation. Evidence of soft sediment deformation at the contact between the Bråvika Member and Wilsonbreen Formation at Gimleodden (Fig. 4I) is also consistent with the Bråvika Member being unconsolidated during the Marinoan glaciation.

Integrating microtextural and field observations, we suggest that the Bråvika Member includes aeolian deposition and may represent a syn-glacial aeolian sand sea contemporaneous with the Marinoan glaciation. This setting is akin to previously identified Marinoan syn-glacial ergs in the Bakoye Formation of Mali (Deynoux et al. 1989) and the Whyalla Sandstone (Elatina glaciation) of South Australia (Williams 1998; Rose et al. 2013; Ewing et al. 2014). Hoffman and Li (2009) suggested that katabatic winds coming off of the Marinoan ice sheet are the primary transport mechanism for these syn-glacial ergs. The northward paleoflow direction of the Bråvika Member and the Bråvika Member's reciprocal thickness relationship with the Wilsonbreen Formation (Halverson et al. 2004) may reflect this transport mechanism, where a northward-advancing ice margin represented by the Wilsonbreen Formation drives the Bråvika Member to the north with katabatic winds coming off of the Marinoan ice sheet.

The microtextural samples analyzed in this study are specific to the interval in Buldrevågen that is proximal to the Wilsonbreen contact. Given the wide range of possible facies proposed by Halverson et al. (2004), Halverson (2011), Hoffman et al. (2012), and this study, the

Bråvika Member may represent multiple depositional environments across localities that capture a transition from the Cryogenian interglacial to the Marinoan pan-glaciation.

Important questions remain about the apportionment of time within the strata that record the Cryogenian interglacial in Svalbard. The absence of the pre-Marinoan Trezona negative $\delta^{13}C$ excursion below the Wilsonbreen Formation has been used to suggest that the sedimentary package between the Petrovbreen Member and the Wilsonbreen Formation is top-truncated (Hoffman et al. 2012; Fairchild et al. 2016; Halverson et al. 2018). The locations of the hiatal surfaces within the Bråvika Member remain ambiguous, and their locations are critical to understanding the apportionment of time in these units and in the interglacial. Our work would suggest that the uppermost aeolian deposition within the Bråvika Member is continuous with the start of Wilsonbreen deposition, but there may be important hiatal surfaces lower in the Bråvika Member.

## CONCLUSIONS

Quartz surface microtextures preserve the transport histories of modern and ancient sediment. However, because workers count microtextures differently for samples from the same depositional environment, the defining microtextures of certain transport modes are not well constrained. We used PCA to directly compare quantitative microtextural data from modern and ancient aeolian, fluvial, and glacial sediments across workers. Although differences between workers are the largest sources of variance in the dataset, the PCA ordinations show that aeolian samples are microtexturally distinct from fluvial and glacial samples across studies. Fluvial and glacial samples are difficult to disambiguate from each other in this dataset, suggesting that sediment from fluvial and glacial environments are microtexturally similar. The PCA ordinations also demonstrate that ancient sediments and modern sediments have quantitatively similar microtextural relationships. Therefore, PCA may be a useful tool to elucidate the ambiguous transport histories of some ancient sediment grains. As a test case, we used the PCA ordinations to constrain the depositional environment of the ambiguous Cryogenian Bråvika Member from Svalbard. These PCA ordinations, combined with field observations, indicate that the Bråvika Member includes aeolian deposition, and suggest that the Bråvika Member may be analogous to syn-glacial Marinoan aeolian sand seas such as the Bakoye Formation in Mali and the Whyalla Sandstone in South Australia. This study demonstrates that PCA can identify microtextures that distinguish sedimentary environments across multiple studies, which in turn helps constrain the depositional history of ambiguous sedimentary deposits like the Bråvika Member.

## SUPPLEMENTARY MATERIAL

All supplementary materials related to this study—including code, raw microtextural data, and SEM images— are available at https://github.com/jreahl/Reahl_2020. The supplementary figures and tables referenced in this manuscript are located at the end of this document.

## LAND ACKNOWLEDGEMENT

This work—from analysis to writing—was performed at institutions built on Indigenous land, using samples collected from Indigenous lands. As geoscientists in a community where only 14% of PhD recipients in the geosciences are from underrepresented minorities (Bernard and Cooperdock 2018), we feel it necessary to acknowledge the Indigenous Peoples as the traditional stewards of the lands that we live and work on. The samples analyzed for the first time in this study were collected from the traditional and ancestral territories of the Cocopah (*Kwapa*), Kumeyaay, Salt River O'odham (Pima) and Piipaash (Maricopa), Quechan (*Kwatsáan*), Comanche (*Nʉmʉnʉʉ*), Kiowa (*[Gáui[dòñ:gyà*), Osage (*Wahzhazhe*), Wichita (*Kirikirʔi:s*), Waco (*Wí:koʔ*), Keechi (*Ki:che:ss*), Tawakoni (*Tawá:kharih*), and Taku River Tlingit (*Lingít*). Laboratory analysis and SEM analysis was performed on unceded Wampanoag land. Writing was performed on the territories of the Abenaki, Chumash, and Wampanoag. We acknowledge the painful history of genocide and forced removal inflicted on these communities and we gratefully acknowledge all of these communities for their past and continued stewardship of these lands. We also acknowledge the dispossession of Indigenous land through the 1862 Morrill Act, which turned parcels of land taken from tribal nations into seed money for land-grant universities like the Massachusetts Institute of Technology. We encourage readers to engage with Indigenous communities and cultures around where they live and work. The Native Land Digital database (native-land.ca) is an excellent resource to begin this process. The best resources for prolonged learning are through direct conversation and collaboration with Indigenous community members. Many Indigenous communities have dedicated cultural heritage officers who may be available as partners in these efforts; the National Congress of American Indians (ncai.org) hosts a tribal directory with contact information.

## ACKNOWLEDGEMENTS

We thank the Salt River Pima-Maricopa Indian Community Cultural Resource Department, Justin Brundin (Cultural Resources Manager, Cocopah Indian Tribe), Andrea A. Hunter (Tribal Historic Preservation Officer, Osage Nation), Gary McAdams (Cultural Planner, Wichita and Affiliated Tribes), and Benjamin Louter (Heritage Coordinator, Taku River Tlingit First Nation) for assistance with acknowledging Indigenous territory. Adam B. Jost (Massachusetts Institute of Technology) performed field work in Svalbard with M.D.C., J.W., T.J.M., and K.D.B.; collected photographs; and trained and assisted J.N.R. in the laboratory. We thank Steven M. Adams and Gerilyn S. Soreghan (University of Oklahoma) for collecting and providing samples from the Algodones Dunes and the Waynoka Dunes. The Juneau Icefield Research Program (JIRP), Foundation for Glacier and Environmental Research (FGER), and Coastal Helicopters in Juneau, Alaska provided logistical support, food, and lodging on the Juneau Icefield. This work began as J.N.R.'s undergraduate thesis project at Wellesley College. We thank Daniel J. Brabander, Katrin Monecke, and Wesley A. Watters at Wellesley College for being on the thesis committee. We thank Timothy J. Cavanaugh at the Harvard University Center for Nanoscale Systems (CNS) for assistance operating the SEM. The Harvard CNS is a member of the National Nanotechnology Coordinated Infrastructure Network (NNCI), which is supported by the National Science Foundation under NSF award no. 1541959. K.D.B. acknowledges support from the Victor P. Starr Development Chair and the David and Lucille Packard Foundation. M.D.C. received support from a National Defense Science and Engineering Graduate Fellowship. J.W. received support from the Dean of the School of Science Fellowship at MIT. T.J.M. received support from the Agouron Geobiology Institute. Field work in Svalbard was supported by the MIT Wade Fund awarded to K.D.B. Field work on the Juneau Icefield was partially funded by the National Association of Geoscience Teachers (NAGT) Scholarship for Field Study awarded to J.N.R.

## AUTHOR CONTRIBUTIONS

J.N.R. wrote the manuscript, collected samples from the Juneau Icefield, performed SEM analysis on all samples, and performed the PCA analysis. M.D.C. and K.D.B. were the primary advisors to J.N.R. J.W. shared her stratigraphic columns and samples of the Bråvika Member, as well as insight on statistics and machine learning. J.W., M.D.C., T.J.M., and K.D.B. characterized and collected samples of the Bråvika Member in Svalbard during their 2017 field season. T.J.M. contributed samples from the McMurdo Dry Valleys. All authors reviewed the final manuscript.

## REFERENCES

Adams, S.A., 2018, Evaluating desert silt production using field, experimental, and remote-sensing methods. [Thesis]: University of Oklahoma, Norman, Oklahoma.

Adams, S.M. and Soreghan, G.S., 2020, A test of the efficacy of sand saltation for silt production: Implications for the interpretation of loess: Geology, v. 28, p. 1–5.

Axen, G.J. and Fletcher, J.M., 1998, Late Miocene-Pleistocene extensional faulting, northern gulf of California, Mexico and Salton Trough, California: International Geology Review, v. 40, p. 217–244.

Bernard, R.E. and Cooperdock, E.H.G., 2018, No progress on diversity in 40 years: Nature Geoscience, v. 11, p. 292–295.

Blackwelder, P.L. and Pilkey, O.H., 1972, Electron microscopy of quartz grain surface textures: the U.S. eastern Atlantic continental margin: Journal of Sedimentary Petrology, v. 42, p. 520–526.

Brew, D.A., Karl, S.M., Barnes, D.F., Jachens, R.C., Ford, A.B. and Horner, R., 1991, A northern Cordilleran ocean-continent transect: Sitka Sound, Alaska, to Atlin Lake, British Columbia: Canadian Journal of Earth Sciences, v. 28, p. 840–853.

Browne, G.H. and Naish, T.R., 2003, Facies development and sequence architecture of a late Quaternary fluvial-marine transition, Canterbury Plains and shelf, New Zealand: Implications for forced regressive deposits: Sedimentary Geology, v. 158, p. 57–86.

Bull, P.A., 1981, Environmental reconstruction by electron microscopy: Progress in Physical Geography, v. 5, p. 368–397.

Calver, C.R., Crowley, J.L., Wingate, M.T.D., Evans, D.A.D., Raub, T.D. and Schmitz, M.D., 2013, Globally synchronous Marinoan deglaciation indicated by U-Pb geochronology of the Cottons Breccia, Tasmania, Australia: Geology, v. 41, p. 1127–1130.

Clague, J.J., Koch, J. and Geertsema, M., 2010, Expansion of outlet glaciers of the Juneau icefield in northwest British Columbia during the past two millennia: Holocene, v. 20, p. 447–461.

Coch, N.K. and Krinsley, D.H., 1971, Comparison of stratigraphic and electron microscopic studies in Virginia Pleistocene coastal sediments: Journal of Geology, v. 79, p. 426–437.

Costa, P.J.M., Andrade, C., Dawson, A.G., Mahaney, W.C., Freitas, M.C., Paris, R. and Taborda, R., 2012, Microtextural characteristics of quartz grains transported and deposited by tsunamis and storms: Sedimentary Geology, v. 275–276, p. 55–69.

Costa, P.J.M., Andrade, C., Mahaney, W.C., Marques da Silva, F., Freire, P., Freitas, M.C., Janardo, C., Oliveira, M.A., Silva, T. and Lopes, V., 2013, Aeolian microtextures in silica spheres induced in a wind tunnel experiment: Comparison with aeolian quartz: Geomorphology, v. 180–181, p. 120–129.

Costa, P.J.M., Park, Y.S., Kim, Y. Do, Quintela, M., Mahaney, W.C., Dourado, F. and Dawson, S., 2017, Imprints in silica grains induced during an open-channel flow experiment: Determination of microtextural signatures during aqueous transport: Journal of Sedimentary Research, v. 87, p. 677–687.

Culver, S.J., Bull, P.A., Campbell, S., Shakesby, R.A. and Whalley, W.B., 1983, Environmental discrimination based on quartz grain surface textures: a statistical investigation: Sedimentology, v. 30, p. 129–136.

Deane, S.M., 2010, Quartz grain microtextures and sediment provenance: using scanning electron microscopy to characterize tropical highland sediments from Costa Rica and the Dominican Republic. [Thesis]: University of Tennessee.

Derickson, D., Kocurek, G., Ewing, R.C. and Bristow, C., 2008, Origin of a complex and spatially diverse dune-field pattern, Algodones, southeastern California: Geomorphology, v. 99, p. 186–204.

Deynoux, M., Kocurek, G. and Proust, J.N., 1989, Late Proterozoic periglacial aeolian deposits on the West African Platform, Taoudeni Basin, western Mali: Sedimentology, v. 36, p. 531–549.

Ewing, R.C., Eisenman, I., Lamb, M.P., Poppick, L., Maloof, A.C. and Fischer, W.W., 2014, New constraints on equatorial temperatures during a Late Neoproterozoic snowball Earth glaciation: Earth and Planetary Science Letters, v. 406, p. 110–122.

Fairchild, I.J., Bonnand, P., Davies, T., Fleming, E.J., Grassineau, N., Halverson, G.P., Hambrey, M.J., McMillan, E.M., McKay, E., Parkinson, I.J. and Stevenson, C.T.E., 2016, The Late Cryogenian Warm Interval, NE Svalbard: Chemostratigraphy and genesis: Precambrian Research, v. 281, p. 128–154.

Folk, R.L., 1980, Petrology of Sedimentary Rocks *in*: Hemphill Publishing Company, Austin, Texas.

Frontier, S., 1976, Étude de la décroissance des valeurs propres dans une analyse en composantes principales: comparison avec le modéle du bâton brisé: Journal of Experimental Marine Biology, v. 25, p. 67–75.

Fryberger, S.G. and Schenk, C.J., 1988, Pin stripe lamination: a distinctive feature of modern and ancient aeolian sediments: Sedimentary Geology, v. 55, p. 1–15.

Garzanti, E., Resentini, A., Andò, S., Vezzoli, G., Pereira, A. and Vermeesch, P., 2015, Physical controls on sand composition and relative durability of detrital minerals during ultra-long distance littoral and aeolian transport (Namibia and southern Angola): Sedimentology, v. 62, p. 971–996.

Garzanti, E., 2017, The maturity myth in sedimentology and provenance analysis: Journal of Sedimentary Research, v. 87, p. 353–365.

Goldstein, J.I., Newbury, D.E., Echlin, P., Joy, D.C., Romig Jr., A.D., Lyman, C.E., Fiori, C. and Lifshin, E., 1992, Scanning Electron Microscopy and X-Ray Microanalysis *in*: Springer, Boston, Massachusetts.

Gumbley, J.W., 1975, A sedimentological study of three saline lakes in the Dry Valleys of Victoria Land, Antarctica. [Thesis]: University of Waikato.

Halverson, G.P., Maloof, A.C. and Hoffman, P.F., 2004, The Marinoan glaciation (Neoproterozoic) in northeast Svalbard: Basin Research, v. 16, p. 297–324.

Halverson, G.P., 2011, Glacial sediments and associated strata of the Polarisbreen Group, northeastern Svalbard *in*: Arnaud, E. et al., eds., The Geological Record of Neoproterozoic Glaciations. The Geological Society of London, London, United Kingdom, v. 36, p. 571–579.

Halverson, G.P., Kunzmann, M., Strauss, J. V. and Maloof, A.C., 2018, The Tonian-Cryogenian transition in Northeastern Svalbard: Precambrian Research, v. 319, p. 79–95.

Hoffman, P.F. and Li, Z.X., 2009, A palaeogeographic context for Neoproterozoic glaciation: Palaeogeography, Palaeoclimatology, Palaeoecology, v. 277, p. 158–172.

Hoffman, P.F., Halverson, G.P., Domack, E.W., Maloof, A.C., Swanson-Hysell, N.L. and Cox, G.M., 2012, Cryogenian glaciations on the southern tropical paleomargin of Laurentia (NE Svalbard and East Greenland), and a primary origin for the upper Russøya (Islay) carbon isotope excursion: Precambrian Research, v. 206–207, p. 137–158.

Immonen, N., 2013, Surface microtextures of ice-rafted quartz grains revealing glacial ice in the Cenozoic Arctic: Palaeogeography, Palaeoclimatology, Palaeoecology, v. 374, p. 293–302.

Jackson, D.A., 1993, Stopping rules in principal components analysis: a comparison of heuristical and statistical approaches: Ecology, v. 74, p. 2204–2214.

Janitsky, P., 1986, Citrate-bicarbonate-dithionite (CBD) extractable iron and aluminum *in*: Singer, M. J., and Janitsky, P., eds., Field and laboratory procedures used in a soil chronosequence study 1648th edn. U.S. Geological Survey Bulletin, p. 38–41.

Jungblut, A.D., Hawes, I., Mackey, T.J., Krusor, M., Doran, P.T., Sumner, D.Y., Eisen, J.A., Hillman, C. and Goroncy, A.K., 2016, Microbial mat communities along an oxygen gradient in a perennially ice-covered Antarctic lake: Applied and Environmental Microbiology, v. 82, p. 620–630.

Kalińska-Nartiša, E., Lamsters, K., Karušs, J., Krievāns, M., Rečs, A. and Meija, R., 2017, Quartz grain features in modern glacial and proglacial environments: A microscopic study from the Russell Glacier, southwest Greenland: Polish Polar Research, v. 38, p. 265–289.

Keiser, L.J., Soreghan, G.S. and Kowalewski, M., 2015, Use of quartz microtextural analysis to assess possible proglacial deposition for the Pennsylvanian–Permian Cutler Formation (Colorado, U.S.A.): Journal of Sedimentary Research, v. 85, p. 1310–1322.

Kendall, B., Creaser, R.A. and Selby, D., 2006, Re-Os geochronology of postglacial black shales in Australia: Constraints on the timing of ‘Sturtian’ glaciation: Geology, v. 34, p. 729–732.

Kocurek, G. and Fielder, G., 1982, Adhesion structures: Journal of Sedimentary Petrology, v. 52, p. 1229–1241.

Krinsley, D.H. and Takahashi, T., 1962, Applications of electron microscopy to geology: Transactions of the New York Academy of Sciences, v. 25, p. 3–22.

Krinsley, D.H. and Funnell, B.M., 1965, Environmental history of quartz sand grains from the Lower and Middle Pleistocene of Norfolk, England: Quarterly Journal of the Geological

Society of London, v. 121, p. 435–456.

Krinsley, D.H. and Doornkamp, J.C., 1973, Atlas of Sand Grain Surface Textures *in*: Cambridge University Press, Cambridge, U.K.

Krinsley, D.H. and Trusty, P., 1985, Environmental interpretation of quartz grain surface textures *in*: Zuffa, G. G., ed., Provenance of Arenites, v. 148. Springer, Dordrecht.

Křížek, M., Krbcová, K., Mida, P. and Hanáček, M., 2017, Micromorphological changes as an indicator of the transition from glacial to glaciofluvial quartz grains: Evidence from Svalbard: Sedimentary Geology, v. 358, p. 35–43.

Legendre, P. and Legendre, L., 1998, Numerical ecology *in*: Elsevier Science BV, Amsterdam, The Netherlands.

Lepper, K. and Scott, G.F., 2005, Late Holocene aeolian activity in the Cimarron River valley of west-central Oklahoma: Geomorphology, v. 70, p. 42–52.

Lindé, K. and Mycielska-Dowgiałło, E., 1980, Some experimentally produced microtextures on grain surfaces of quartz sand: Geografiska Annaler. Series A, Physical Geography, v. 62, p. 171–184.

Mackey, T.J., Sumner, D.Y., Hawes, I., Jungblut, A.D. and Andersen, D.T., 2015, Growth of modern branched columnar stromatolites in Lake Joyce, Antarctica: Geobiology, v. 13, p. 373–390.

Mackey, T.J., Sumner, D.Y., Hawes, I. and Jungblut, A.D., 2017, Morphological signatures of microbial activity across sediment and light microenvironments of Lake Vanda, Antarctica: Sedimentary Geology, v. 361, p. 82–92.

Madole, R.F., Ferring, C.R., Guccione, M.J., Hall, S.A., Johnson, W.C. and Sorenson, C.J., 1991, Quaternary geology of the Osage Plains and Interior Highlands *in*: Morrison, R. B., ed., Quaternary Nonglacial Geology: Coterminous U.S. K-2. Geological Society of America, Boulder, Colorado, p. 503–546.

Mahaney, W.C. and Kalm, V., 1995, Scanning electron microscopy of Pleistocene tills in Estonia: Boreas, v. 24, p. 13–29.

Mahaney, W.C., Claridge, G. and Campbell, I., 1996, Microtextures on quartz grains in tills from Antarctica: Palaeogeography, Palaeoclimatology, Palaeoecology, v. 121, p. 89–103.

Mahaney, W.C. and Kalm, V., 2000, Comparative scanning electron microscopy study of oriented till blocks, glacial grains and Devonian sands in Estonia and Latvia: Boreas, v. 29, p. 35–51.

Mahaney, W.C., Stewart, A. and Kalm, V., 2001, Quantification of SEM microtextures useful in sedimentary environmental discrimination: Boreas, v. 30, p. 165–171.

Mahaney, W.C., 2002, Atlas of Sand Grain Surface Textures and Applications *in*: Oxford University Press, New York, New York.

Margolis, S. V. and Krinsley, D.H., 1971, Submicroscopic frosting on eolian and subaqueous quartz sand grains: Bulletin of the Geological Society of America, v. 82, p. 3395–3406.

Margolis, S. V. and Krinsley, D.H., 1974, Processes of formation and environmental occurrence of microfeatures on detrital quartz: American Journal of Science, v. 274, p. 449–464.

McCoy, F.W., Nokleberg, W.J. and Norris, R.M., 1967, Speculations on the origin of the Algodones Dunes, California: Geological Society of America Bulletin, v. 78, p. 1039–1044.

Muhs, D.R., Bush, C.A., Cowherd, S.D. and Mahan, S., 1995, Geomorphic and geochemical evidence for the source of sand in the Algodones Dunes, Colorado Desert, Southeastern California *in*: Tchakerian, V. P., ed., Desert Aeolian Processes. Springer US, Dordrecht, p. 37–74.

Nartišs, M. and Kalińska-Nartiša, E., 2017, An aeolian or a glaciolacustrine record? A case study from Mieļupīte, Middle Gauja Lowland, northeast Latvia: Geologos, v. 23, p. 15–28.

Nedell, S.S., Andersen, D.W., Squyres, S.W. and Love, F.G., 1987, Sedimentation in ice-covered Lake Hoare, Antarctica: Sedimentology, v. 34, p. 1093–1106.

Nieter, W.M. and Krinsley, D.H., 1976, The production and recognition of aeolian features on sand grains by silt abrasion: Sedimentology, v. 23, p. 713–720.

Norris, R.M. and Norris, K.S., 1961, Algodones Dunes of Southeastern California: Geological Society of America Bulletin, v. 72, p. 605–620.

Pedregosa, F., Varoquaux, G., Gramfort, A., Michel, V., Thirion, B., Grisel, O., Blondel, M., Prettenhofer, P., Weiss, R., Dubourg, V., Vanderplas, J., Passos, A., Cournapeau, D., Brucher, M., Perrot, M. and Duchesnay, É., 2011, Scikit-learn: Machine Learning in Python: Journal of Machine Learning Research, v. 12, p. 2825–2830.

Peres-Neto, P.R., Jackson, D.A. and Somers, K.M., 2003, Giving meaningful interpretation to ordination axes: assessing loading significance in principal component analysis: Ecology, v. 84, p. 2347–2363.

Pettijohn, F.J., 1957, Paleocurrents of Lake Superior Precambrian Quartzites: Bulletin of the Geological Society of America, v. 68, p. 489–480.

Pippin, M., 2016, Progressive downstream overprinting of glacially induced quartz microtextures during fluvial saltation, Salmon River, British Columbia and Alaska. [Thesis]: Texas Tech University.

Porter, J.J., 1962, Electron microscopy of sand surface texture: Journal of Sedimentary Petrology, v. 32, p. 124–135.

Prave, A.R., Condon, D.J., Hoffmann, K.H., Tapster, S. and Fallick, A.E., 2016, Duration and nature of the end-Cryogenian (Marinoan) glaciation: Geology, v. 44, p. 631–634.

Pye, K., 1983, Coastal Dunes: Progress in Physical Geography, v. 7, p. 531–557.

Pye, K. and Tsoar, H., 2009, Aeolian Sand and Sand Dunes *in*: Springer-Verlag Berlin Heidelberg, Leipzig, Germany.

Rivera-Hernandez, F., Sumner, D.Y., Mackey, T.J., Hawes, I. and Andersen, D.T., 2019, In a PICL: The sedimentary deposits and facies of perennially ice-covered lakes: Sedimentology, v. 66, p. 917–939.

Rogers, B., 2007, Morphology of fixed sand dunes for paleowind reconstruction in northwestern Oklahoma. [Thesis]: Oklahoma State University, Stillwater, Oklahoma.

Rooney, A.D., Strauss, J. V., Brandon, A.D. and Macdonald, F.A., 2015, A Cryogenian chronology: Two long-lasting synchronous Neoproterozoic glaciations: Geology, v. 43, p. 459–462.

Rose, C. V., Maloof, A.C., Schoene, B., Ewing, R.C., Linnemann, U., Hofmann, M. and Cottle, J.M., 2013, The end-Cryogenian glaciation of South Australia: Geoscience Canada, v. 40, p. 256–293.

Runkel, A.C., Mackey, T.J., Cowan, C.A. and Fox, D.L., 2010, Tropical shoreline ice in the late Cambrian: Implications for earth's climate between the Cambrian Explosion and the Great Ordovician Biodiversification Event: GSA Today, v. 20, p. 4–10.

Schelp, C., 2019, An Alternative Way to Plot the Covariance Ellipse: CarstenSchelp.github.io.

Setlow, L.W., 1978, Age determination of reddened coastal dunes in northwest Florida, U.S.A., by use of scanning electron microscopy *in*: Whalley, W. B., ed., Scanning electron microscopy in the study of sediments. Geo Abstracts, Norwich, England, p. 283–305.

Smith, C., Soreghan, G.S. and Ohta, T., 2018, Scanning electron microscope (SEM) microtextural analysis as a paleoclimate tool for fluvial deposits: A modern test: Bulletin of the Geological Society of America, v. 130, p. 1256–1272.

Spigel, R.H. and Priscu, J.C., 1998, Physical liminology of the McMurdo Dry Valleys lakes *in*: Priscu, J. C., ed., Ecosystem Dynamics in a Polar Desert: the McMurdo Dry Valleys, Antarctica 72nd edn. Washington, D.C., p. 153–187.

Stevic, M., 2015, Identification and environmental interpretation of microtextures on quartz grains from aeolian sediments - Brattforsheden and Vittskövle, Sweden. [Thesis]: Lund University, Lund, Sweden.

Sweet, D.E. and Soreghan, G.S., 2010, Application of quartz sand microtextural analysis to infer cold-climate weathering for the equatorial Fountain Formation (Pennsylvanian-Permian, Colorado, U.S.A.): Journal of Sedimentary Research, v. 80, p. 666–677.

Sweet, D.E. and Brannan, D.K., 2016, Proportion of glacially to fluvially induced quartz grain microtextures along the Chitina River, SE Alaska, U.S.A.: Journal of Sedimentary Research, v. 86, p. 749–761.

Van de Kamp, P.C., 1973, Holocene continental sedimentation in the Salton Basin, California: A reconnaissance: Geological Society of America Bulletin, v. 84, p. 827–848.

Vincent, P.J., 1976, Some periglacial deposits near Aberystwyth, Wales, as seen with a scanning electron microscope: Biuletyn Periglacialny, v. 25, p. 59–64.

Vos, K., Vandenberghe, N. and Elsen, J., 2014, Surface textural analysis of quartz grains by scanning electron microscopy (SEM): From sample preparation to environmental interpretation: Earth-Science Reviews, v. 128, p. 93–104.

Waters, M.R., 1983, Late Holocene lacustrine chronology and archaeology of ancient Lake Cahuilla, California: Quaternary Research, v. 19, p. 373–387.

Williams, G.E., 1998, Late Neoproterozoic periglacial aeolian sand sheet, Stuart Shelf, South Australia: Australian Journal of Earth Sciences, v. 45, p. 733–741.

Wilson, I.G., 1972, Aeolian bedforms—their development and origins: Sedimentology, v. 19, p. 173–210.

Winspear, N.R. and Pye, K., 1995, Sand supply to the Algodones dunefield, south-eastern California, USA: Sedimentology, v. 42, p. 875–891.

Woronko, B., 2016, Frost weathering versus glacial grinding in the micromorphology of quartz sand grains: Processes and geological implications: Sedimentary Geology, v. 335, p. 103–119.

Yu, W., Algeo, T.J., Du, Y., Zhou, Q., Wang, P., Xu, Y., Yuan, L. and Pan, W., 2017, Newly discovered Sturtian cap carbonate in the Nanhua Basin, South China: Precambrian Research, v. 293, p. 112–130.

Zhang, S., Jiang, G. and Han, Y., 2008, The age of the Nantuo Formation and Nantuo glaciation in South China: Terra Nova, v. 20, p. 289–294.

**SUPPLEMENTARY MATERIAL**

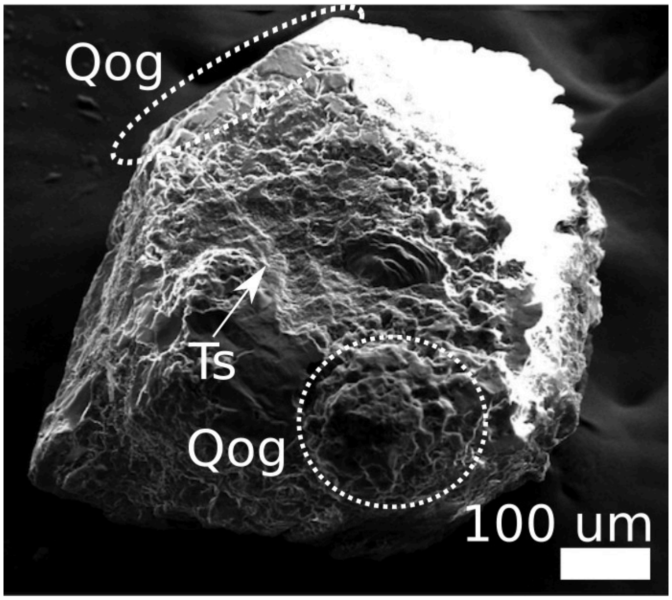


**Figure S1.** Example of a diagenetically overprinted grain with quartz overgrowths (Qog) and turtle-skin silica (Ts). Because quartz overgrowths and turtle-skin silica overprint the original character of the grains, diagenetically-overprinted grains are excluded from SEM analysis.

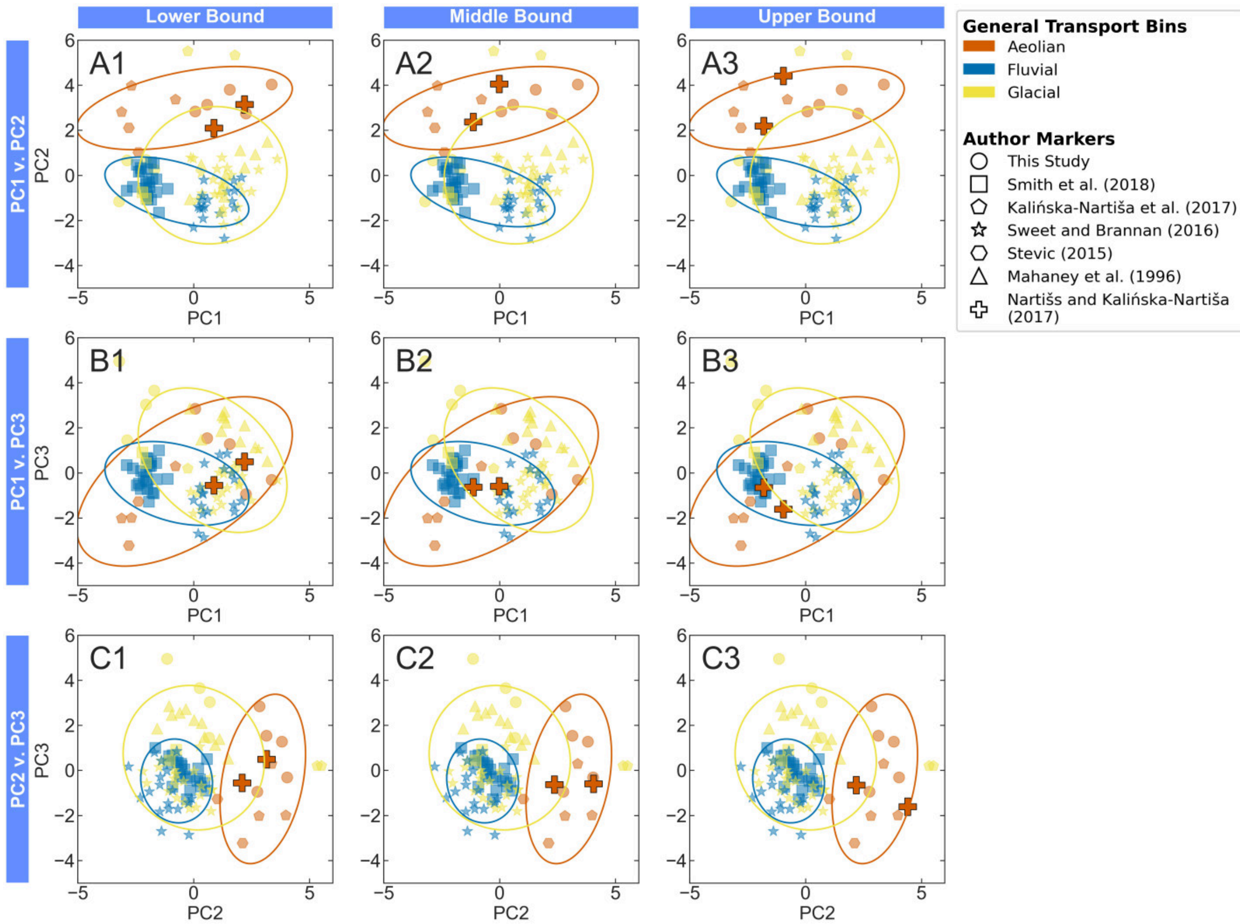


**Figure S2.** All-textures PCA ordination biplots of the ancient Nartišs and Kalińska-Nartiša (2017) samples using the lower (column 1), middle (column 2), and upper bounds (column 3) of each abundance bin in Nartišs and Kalińska-Nartiša (2017). Row A is in PC1-PC2 space, row B is in PC1-PC3 space, and row C is in PC2-PC3 space. The transparent points are the modern samples used in this study (this study through Mahaney et al. 1996). The ellipses are 95% confidence intervals of each modern transport mode that are centered at the mean of the transport mode in each coordinate space. The ellipses are calculated using the methods of Schelp (2019).

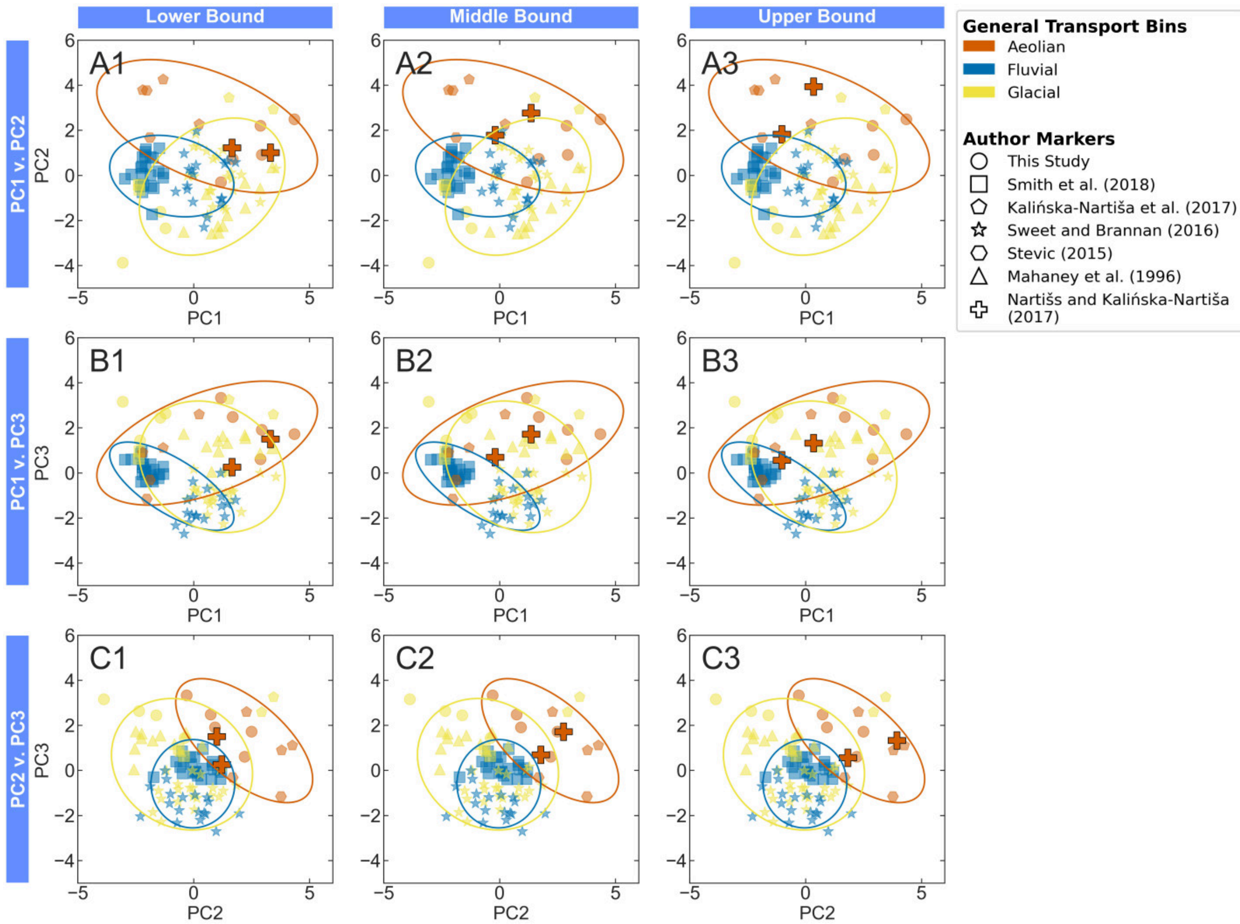


**Figure S3.** Mechanical PCA ordination biplots of the ancient Nartišs and Kalińska-Nartiša (2017) samples using the lower (column 1), middle (column 2), and upper bounds (column 3) of each abundance bin in Nartišs and Kalińska-Nartiša (2017). Row A is in PC1-PC2 space, row B is in PC1-PC3 space, and row C is in PC2-PC3 space. The transparent points are the modern samples used in this study (this study through Mahaney et al. 1996). The ellipses are 95% confidence intervals of each modern transport mode that are centered at the mean of the transport mode in each coordinate space. The ellipses are calculated using the methods of Schelp (2019).

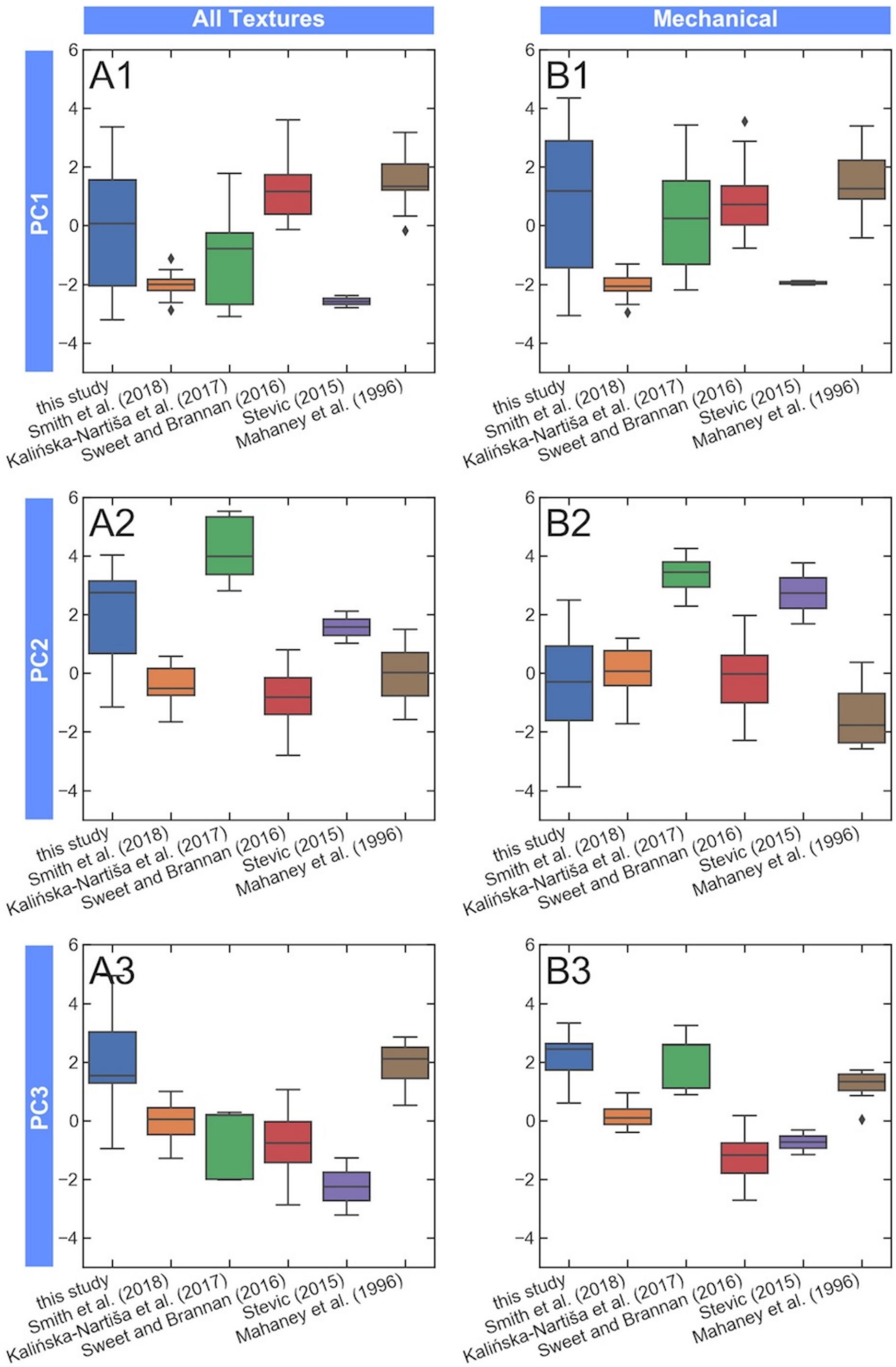


**Figure S4.** Boxplots of the modern samples grouped by author in the all-textures PCA ordination (column A) and the mechanical ordination (column B). Each column represents a principal component axis in each ordination: PC1 (row 1), PC2 (row 2), and PC3 (row 3). The small black diamonds represent modern outliers for each transport mode.

**Table S1.** Microtextural comparison table of all the studies with modern samples considered in this work. Microtextures with no analog to the microtextures analyzed in this study are marked with "N/A".

| Citation | | This study | Smith et al. (2018) | Kalińska-Nartiša et al. (2017) | Sweet and Brannan (2016) | Stevic (2015) | Mahaney et al. (1996) |
|---|---|---|---|---|---|---|---|
| Microtexture Analogs | Polygenetic | abrasion features | abrasion features | abrasion fatigue | N/A | abraded edges | abrasion features |
| | | arc-shaped steps | arc-shaped steps | arcuate steps | arc-shaped steps | arcuate steps | arc-shaped steps |
| | | breakage blocks | breakage blocks | breakage blocks | breakage blocks | breakage blocks small | N/A |
| | | conchoidal fractures | conchoidal fractures | conchoidal fractures <100 | conchoidal fractures | conchoidal (<100μm) | conchoidal fractures |
| | | fracture faces | fracture faces | N/A | fracture faces | flat cleavage surfaces | fracture faces |
| | | linear steps | linear steps | straight steps | linear steps | straight steps | linear steps |
| | | sharp angular features | sharp angular features | angular grains | sharp angular features | angular | sharp angular features |
| | | subparallel linear fractures | subparallel linear fractures | parallel striations | subparallel linear fractures | parallel striations | subparallel linear fractures |
| | | upturned plates | upturned plates | N/A | mechanically upturned plates | upturned plates | mechanically upturned plates |
| | Percussion | edge rounding | edge rounding | bulbous edges | edge rounding | bulbous edges | edge rounding |
| | | v-shaped percussion cracks | v-shaped percussion cracks | v-shaped cracks | v-shaped cracks | v-shaped cracks | v-shaped percussion cracks |
| | High-Stress | crescentic gouges | crescentic gouges | N/A | crescentic gouges | N/A | crescentic gouges |
| | | curved grooves | curved grooves | straight/curved grooves | curved grooves | straight/curved grooves | curved grooves |
| | | deep troughs | deep troughs | N/A | deep troughs | N/A | deep troughs |
| | | straight grooves | straight grooves | N/A | straight grooves | N/A | straight grooves |
| | Chemical | dissolution etching | dissolution etching | solution pits | N/A | solution pits | dissolution etching |
| | | precipitation features | precipitation features | precipitation | precipitation features | precipitation | precipitation features |
| | General | low relief | low relief | low relief | low relief | low relief | low relief |
| | | medium relief | medium relief | medium relief | medium relief | medium relief | medium relief |
| | | high relief | high relief | high relief | high relief | high relief | high relief |

**Table S2.** Microtextural comparison table of all the studies with ancient samples considered in this work. Microtextures with no analog to the microtextures analyzed in this study are marked with “N/A”.

| | Citation | This study | Nartišs and Kalińska-Nartiša (2017) | Deane (2010) | Sweet and Soreghan (2010) | Mahaney et al. (2001) | Mahaney and Kalm (1995) |
|---|---|---|---|---|---|---|---|
| Microtexture Analogs | Polygenetic | abrasion features | abrasion fatigue | abrasion | abrasion features | abrasion features | abrasion features |
| | | arc-shaped steps | arcuate steps | arc-shaped steps | arc-shaped steps | arc-shaped steps | arc-shaped steps |
| | | breakage blocks | N/A | breakage blocks | breakage blocks | N/A | N/A |
| | | conchoidal fractures | conchoidal features (<100µm) | conchoidal fractures | conchoidal fractures | conchoidal fractures | conchoidal fractures |
| | | fracture faces | N/A | fracture faces | fracture faces | fracture faces | fracture faces |
| | | linear steps | straight steps | linear steps | linear steps | linear steps | linear steps |
| | | sharp angular features | angular outline | sharp, angular features | sharp angular features | sharp angular features | sharp angular features |
| | | subparallel linear fractures | parallel striations | sub-parallel linear fractures | subparallel linear fractures | subparallel linear fractures | subparallel linear fractures |
| | | upturned plates | upturned plates | mechanically upturned plates | mechanically upturned plates | mechanically upturned plates | mechanically-upturned plates |
| | Percussion | edge rounding | bulbous edges | edge rounding | edge rounding | edge rounding | edge rounding |
| | | v-shaped percussion cracks | v-shaped percussion cracks | v-shaped percussion fractures | v-shaped percussion cracks | v-shaped percussion cracks | v-shaped percussion cracks |
| | High-Stress | crescentic gouges | N/A | crescentic gouges | crescentic gouges | crescentic gouges | crescentic gouges |
| | | curved grooves | straight/curved grooves | curved grooves | curved grooves | curved grooves | curved grooves |
| | | deep troughs | N/A | deep troughs | deep troughs | deep troughs | deep troughs |
| | | straight grooves | N/A | straight grooves | straight grooves | straight grooves | straight grooves |
| | Chemical | dissolution etching | solution pits | dissolution etching | dissolution etching | dissolution etching | dissolution etching |
| | | precipitation features | precipitation | precipitation | N/A | precipitation features | precipitation features |
| | General | low relief | low relief | low relief | low relief | low relief | low relief |
| | | medium relief | medium relief | medium relief | medium relief | medium relief | medium relief |
| | | high relief | high relief | high relief | high relief | high relief | high relief |

**Table S3.** First quartiles (q25), medians (q50), third quartiles (q75), lower adjacent values (h1), and upper adjacent values (h2) of modern aeolian, fluvial, and glacial samples along PC1, PC2, and PC3 in the all-textures and mechanical PCA ordinations.

| Ordination | PC | Transport Mode | q25 | q50 | q75 | h1 | h2 |
|---|---|---|---|---|---|---|---|
| All Textures | PC1 | Aeolian | -2.6 | -0.4 | 1.3 | -3.1 | 3.4 |
| | | Fluvial | -2.0 | -1.6 | 0.4 | -2.9 | 2.1 |
| | | Glacial | 0.2 | 1.2 | 1.9 | -2.2 | 3.6 |
| | PC2 | Aeolian | 2.8 | 3.0 | 3.7 | 2.1 | 4.0 |
| | | Fluvial | -1.2 | -0.7 | -0.2 | -2.3 | 0.6 |
| | | Glacial | -0.8 | -0.2 | 0.7 | -2.2 | 1.5 |
| | PC3 | Aeolian | -1.8 | -0.6 | 1.0 | -3.2 | 2.8 |
| | | Fluvial | -0.9 | -0.4 | 0.3 | -2.7 | 1.0 |
| | | Glacial | -0.6 | 0.2 | 1.5 | -1.8 | 3.7 |
| Mechanical | PC1 | Aeolian | -1.7 | 0.7 | 2.6 | -2.2 | 4.3 |
| | | Fluvial | -2.1 | -1.5 | 0.0 | -3.0 | 1.8 |
| | | Glacial | 0.1 | 1.0 | 1.6 | -1.4 | 3.6 |
| | PC2 | Aeolian | 1.1 | 2.2 | 3.4 | -0.3 | 4.3 |
| | | Fluvial | -0.6 | 0.1 | 0.6 | -2.3 | 2.0 |
| | | Glacial | -1.5 | -0.6 | 0.3 | -3.9 | 2.9 |
| | PC3 | Aeolian | 0.7 | 1.4 | 2.3 | -1.1 | 3.3 |
| | | Fluvial | -1.4 | -0.3 | 0.1 | -2.7 | 0.9 |
| | | Glacial | -0.9 | 0.0 | 1.4 | -2.3 | 3.3 |

**Table S4.** First quartiles (q25), medians (q50), third quartiles (q75), lower adjacent values (h1), and upper adjacent values (h2) of the modern samples grouped by study along PC1, PC2, and PC3 in the all-textures and mechanical PCA ordinations.

| type | PC | Study | q25 | q50 | q75 | h1 | h2 |
|---|---|---|---|---|---|---|---|
| All Textures | PC1 | this study | -2.1 | 0.1 | 1.6 | -3.2 | 3.4 |
| | | Smith et al. (2018) | -2.2 | -2.0 | -1.8 | -2.6 | -1.5 |
| | | Kalińska-Nartiša et al. (2017) | -2.7 | -0.8 | -0.3 | -3.1 | 1.8 |
| | | Sweet and Brannan (2016) | 0.4 | 1.2 | 1.7 | -0.1 | 3.6 |
| | | Stevic (2015) | -2.7 | -2.6 | -2.5 | -2.8 | -2.4 |
| | | Mahaney et al. (1996) | 1.2 | 1.3 | 2.1 | 0.3 | 3.2 |
| | PC2 | this study | 0.7 | 2.7 | 3.1 | -1.2 | 4.0 |
| | | Smith et al. (2018) | -0.8 | -0.5 | 0.2 | -1.7 | 0.6 |
| | | Kalińska-Nartiša et al. (2017) | 3.4 | 4.0 | 5.3 | 2.8 | 5.5 |
| | | Sweet and Brannan (2016) | -1.4 | -0.8 | -0.2 | -2.8 | 0.8 |
| | | Stevic (2015) | 1.3 | 1.6 | 1.8 | 1.0 | 2.1 |
| | | Mahaney et al. (1996) | -0.8 | 0.0 | 0.7 | -1.6 | 1.5 |
| | PC3 | this study | 1.3 | 1.5 | 3.0 | -0.9 | 4.9 |
| | | Smith et al. (2018) | -0.5 | 0.0 | 0.4 | -1.3 | 1.0 |
| | | Kalińska-Nartiša et al. (2017) | -2.0 | 0.2 | 0.2 | -2.0 | 0.3 |
| | | Sweet and Brannan (2016) | -1.4 | -0.8 | 0.0 | -2.9 | 1.1 |
| | | Stevic (2015) | -2.7 | -2.2 | -1.8 | -3.2 | -1.3 |
| | | Mahaney et al. (1996) | 1.4 | 2.1 | 2.5 | 0.5 | 2.8 |
| Mechanical | PC1 | this study | -1.4 | 1.2 | 2.9 | -3.1 | 4.3 |
| | | Smith et al. (2018) | -2.2 | -2.1 | -1.8 | -2.7 | -1.3 |
| | | Kalińska-Nartiša et al. (2017) | -1.3 | 0.2 | 1.5 | -2.2 | 3.4 |
| | | Sweet and Brannan (2016) | 0.0 | 0.7 | 1.3 | -0.8 | 2.9 |
| | | Stevic (2015) | -2.0 | -2.0 | -1.9 | -2.0 | -1.9 |
| | | Mahaney et al. (1996) | 0.9 | 1.3 | 2.2 | -0.4 | 3.4 |
| | PC2 | this study | -1.6 | -0.3 | 0.9 | -3.9 | 2.5 |
| | | Smith et al. (2018) | -0.4 | 0.1 | 0.8 | -1.7 | 1.2 |
| | | Kalińska-Nartiša et al. (2017) | 2.9 | 3.4 | 3.8 | 2.3 | 4.3 |
| | | Sweet and Brannan (2016) | -1.0 | 0.0 | 0.6 | -2.3 | 2.0 |
| | | Stevic (2015) | 2.2 | 2.7 | 3.2 | 1.7 | 3.8 |
| | | Mahaney et al. (1996) | -2.4 | -1.8 | -0.7 | -2.6 | 0.4 |
| | PC3 | this study | 1.7 | 2.4 | 2.6 | 0.6 | 3.3 |
| | | Smith et al. (2018) | -0.1 | 0.1 | 0.4 | -0.4 | 1.0 |
| | | Kalińska-Nartiša et al. (2017) | 1.1 | 2.6 | 2.6 | 0.9 | 3.3 |
| | | Sweet and Brannan (2016) | -1.8 | -1.2 | -0.8 | -2.7 | 0.2 |
| | | Stevic (2015) | -0.9 | -0.7 | -0.5 | -1.1 | -0.3 |
| | | Mahaney et al. (1996) | 1.0 | 1.3 | 1.6 | 0.9 | 1.7 |